Blended-Wing-Body Regional Aircraft Optimization with High-Fidelity Aerodynamics and Critical Design Requirements

Aiden L. Gray* and David W. Zingg†
University of Toronto, Toronto, Ontario, M3H 5T6, Canada

Conventional tube-and-wing and proposed blended-wing-body airliners must satisfy several design requirements, but the latter configuration is tightly integrated and sensitive to these requirements. In this work, blended-wing-body regional aircraft are investigated using a gradient-based mixed-fidelity multidisciplinary optimization framework centered on a Reynolds-averaged Navier-Stokes solver. In addition to sizing and cruise trim, design requirements considered include one-engine-inoperative directional trim, takeoff rotation ability, takeoff field length, initial climb performance, low-speed trim and static margin, and top-of-climb rate of climb. Results show how optimal design features vary and performance is overpredicted if critical design requirements are excluded and how key elements of geometric freedom help realize the potential of the configuration. A 4.8% block fuel burn benefit is enabled by pivot-piston variable-length landing gear even with low-mounted engines and high design freedom. The off-design constraints penalize block fuel burn by 3.2% if variable-length landing gear is considered, but this value reaches 7.6% if geometric freedom that inhibits tight cabin contouring and the formation of a novel forebody ridge is removed. Leading-edge carving is optimal. The high design freedom and high-fidelity aerodynamics model help efficiently satisfy the design requirements, resulting in a cruise lift-to-drag ratio of 21.7 at 36 000 ft and Mach 0.78.

* Ph.D. Candidate, Institute for Aerospace Studies; aiden.lee@mail.utoronto.ca.
† Distinguished Professor of Computational Aerodynamics and Sustainable Aviation, Institute for Aerospace Studies; david.zingg@utoronto.ca. Associate Fellow AIAA.

Nomenclature

L, D, Y	=	aircraft lift, drag, and side-force
C_L, C_D, C_Y	=	aircraft lift, drag, and side-force coefficients
$l^{(\cdot)}, m^{(\cdot)}, n^{(\cdot)}$	=	aircraft rolling, pitching, and yawing moments about a reference point, $(\cdot)$
$C_l^{(\cdot)}, C_m^{(\cdot)}, C_n^{(\cdot)}$	=	aircraft rolling, pitching, and yawing moment coefficients about a reference point, $(\cdot)$
C_p, C_f	=	pressure and skin-friction coefficients
K_n	=	static margin
T, W	=	thrust, weight
δ_e	=	elevator or flap-elevon deflection angle
V_{EF}, V_1, V_{R}, V_{LOF}, V_{SC}	=	critical engine failure, takeoff decision, rotation, liftoff, and steady-climb speeds
γ_{SC}	=	steady-climb flight path angle
$V_{\mathrm{MC_G}}$, V_2	=	on-ground minimum control, and takeoff safety speeds
V_s	=	reference (level-flight) stall speed without considering the vertical component of thrust
b, c	=	span, chord
L/D	=	lift-to-drag ratio
α	=	angle of attack
y^+	=	nondimensional off-wall distance
x, y, z	=	Cartesian coordinates

I. Introduction

SIGNIFICANT design challenges and financial and technological risks continue to impede industry adoption of efficient unconventional transport aircraft [1]. Although airframe and propulsion technologies have continuously improved over time, a step-change in the former is required to meet industry goals such as net-zero carbon emissions by 2050 [2]. The probability of reaching these goals is increased by pursuing research and development activities related to revolutionary rather than evolutionary designs such as the strut- or truss-braced wing, the blended or hybrid wing-body (BWB or HWB), the box wing, the double bubble, and the flying-V [1].

The BWB aircraft configuration was first conceptualized during the 1980s [3], although the pure flying wing predates it by several decades. Research pertaining to the Boeing BWB-450 aircraft concept is summarized by Liebeck in a 2004 publication [4]; a 450-passenger BWB design was found to have a 15% lower maximum takeoff weight (MTOW) and 27% lower block fuel burn per seat-mile than an equivalent conventional tube-and-wing (CTW, or conventional TAW) aircraft. The BWB configuration is inherently aerodynamically efficient mainly because it can offer a high wetted aspect ratio (wingspan squared over wetted area) for a given internal volume, implying a high maximum lift-to-drag ratio. Indeed, the surface area of a BWB aircraft is lowered by the absence of an empennage and the presence of a smooth blending segment between the centerbody and the wing; moreover, the wingspan of a BWB aircraft can be made larger than that of an equivalently sized CTW aircraft without incurring a wing weight penalty because the thick, structurally efficient, and wide centerbody laterally offsets the wing root.

Thus, the wingspan can be made high relative to the bending span if the practical wingspan limits imposed by airport gate sizes are circumvented through, for example, folding wingtips. Further weight (induced drag) advantages are linked to the absence of an empennage, the low maximum wing bending stress due to the similar spanwise distribution of weight and lifting loads and the partial transfer of lift to the centerbody, and the low fuel weight due to low drag [4].

The literature contains many studies on BWB aircraft that corroborate the advantages discussed above; several are summarized by Bravo-Mosquera et al. [1]. There remains a large variance in published block fuel burn predictions. Assuming optimization is used to assess performance, this variance is due to differences in the objective function, the mission, the technology levels, the design requirements and other constraints, the considered aircraft design disciplines and model fidelity levels, and the type and quantity of design variables. A complete optimization problem formulation would optimize a weighted average objective function accounting for all flyable missions in industry-relevant proportions, integrate the most compatible current or future technologies, solve fully coupled high-fidelity models of every design requirement relevant to aircraft design and certification and consider every relevant discipline, and include many design variables spanning all types. Clearly, the computational cost and complexity of such a problem formulation is intractable. One approach to reducing computational cost and complexity is mixed-fidelity multidisciplinary design optimization (MDO), which is a hybrid approach that can combine low-fidelity conceptual-design equations (with few associated design variables) with medium- to high-fidelity physics-based models (with many associated design variables) and consider only carefully selected critical design requirements. Such numerical optimization frameworks can provide an efficient and adept tool for assessing the performance of unconventional aircraft, as opposed to designing the complete system, if computational resources are strategically allocated mainly where they provide the greatest accuracy benefit. The included medium- to high-fidelity models enable the potential of unconventional aircraft configurations to be realized in part through design features that exploit complex physical phenomena [5–13].

The accuracy of a performance assessment based on mixed-fidelity MDO depends on several factors. Fundamental questions arising during the definition of such an optimization problem may include the following [9], with possible answers discussed in the specific context of BWB aircraft in this paper: 1) Which design requirements are most critical to the accurate determination of the major design features and the accurate estimation of the performance metric? 2) Which aircraft design disciplines, e.g., aerodynamics, structures, mass-property calculations,

propulsion, flight mechanics, are most critical to sufficient model accuracy? 3) Which are the minimum fidelity levels needed to construct accurate and efficient physics-based models of the performance metric and of each design requirement? 4) Which design variables and other constraints enable an optimizer to realize the potential of a given aircraft configuration without introducing unnecessary manufacturing difficulties or inhibiting the convergence of the optimization problem? 5) Must all design variables and relevant design requirements be considered simultaneously during optimization, or can similar conclusions be reached at a lower problem cost and complexity through a sequential or decoupled treatment?

Numerical optimization frameworks are particularly adept at designing the complex multifunctional aerodynamic surfaces required for BWB aircraft; see, for example, Refs. [6–9,14–18]. Published performance assessments range from conceptual-design works to mixed-fidelity MDO that include a computational-fluid-dynamics (CFD) model based on the Reynolds-averaged Navier-Stokes (RANS) equations [1]. The Ascent 1000 BWB designed by DZYNE Technologies, which is now being developed by JetZero, achieves NASA's New Aviation Horizons Ultra-Efficient Subsonic Transport strategic goals for reduced emissions, fuel burn, and noise levels at level N+2, and it has reached a relatively high technology readiness level [18]. The block fuel burn benefit per seat-mile of this regional-class BWB aircraft is estimated through mixed-fidelity MDO to be 62% relative to the Embraer E190AR best-in-class aircraft from 2005. Moreover, the benefit for a single-aisle-class aircraft is 55% when compared to the Boeing 737-800IWG. In the twin-aisle class, a NASA conceptual-level performance assessment estimates the block fuel burn benefit of a BWB aircraft comparably sized to a Boeing 777-200LR to be 54% on a seat-mile basis [19]. A portion of the cited fuel-efficiency benefits are due to the efficient unconventional configuration alone, and the rest is attributed to compatible future technologies, some of which can be synergistic.

Given the high degree of configuration integration characteristic of BWB aircraft, accurate performance assessments typically consider stability and control (S&C) constraints in addition to necessary lift and pitch trim constraints. Lyu and Martins [20] imposed constraints on trim and center of gravity (CG) location in a single-point twist and section-shape optimization of the Boeing BWB-450 based on the RANS equations showing a 0.36% increase in trimmed cruise drag per unit percent-MAC increase in the static margin near neutral stability; a negative static margin typically makes a BWB aircraft more efficient due to lower trim drag [4,6]. The short-coupled nature of BWB pitch control surfaces can imply high overall design sensitivity to low-speed trim and controllability. Accordingly, considerable work has been done to study this aspect of their design. Méheut et al. [17] performed

aerodynamic shape optimization of the AVECA BWB aircraft while enforcing cruise trim constraints and ensuring that rotation is achievable through a low-speed pitching moment constraint. Cruise performance was found to be unaffected by the latter constraint on this twin-aisle BWB aircraft at the selected takeoff rotation speed. Reist and Zingg studied the impact of allowing a negative cruise static margin to increase the fuel efficiency of a regional-class BWB aircraft [6]. Reist et al. [7] studied the influence of several simultaneously enforced S&C requirements on the optimal shape and performance of regional-class BWB aircraft. The aircraft was trimmed, and its static margin was limited at cruise, directional trim was achieved on the ground under one-engine-inoperative (OEI) conditions using fin- or winglet-mounted rudders, and nearly-full-span pitch control surfaces were sized to ensure sufficient control authority to initiate takeoff rotation at a target speed. All constraints were satisfied, but the rotation constraint led to an 8.4% and 4.2% penalty in block fuel burn and MTOW, respectively, and the optimized designs were highly unstable at low speeds. The requirement of directional control authority at low speed was found to be particularly challenging for the X-48B BWB aircraft despite its use of both winglet-mounted rudders and outboard split elevons [21]. Cook and de Castro [22] studied the static and dynamic S&C characteristics of a large BWB aircraft. The limited static margin range in which longitudinal trim could be achieved at low speed was highlighted. Garmendia et al. [23] concluded that using three elevons of unequal span fractions per wing leads to a reduction in control-system weight and power usage and a small block fuel burn benefit over configurations with a larger number of elevons, with the superior configuration having one longer outboard elevon and two shorter inboard elevons.

Despite ample interest in the BWB concept [4,17,21,24–27], only a small proportion of projects have focused on regional- or single-aisle-class airliners. There has been some doubt that the BWB configuration is significantly advantageous in the smaller aircraft classes; see, for example Ref. [28,29]. After finding that the classical wide-centerbody BWB planform is suboptimal for regional-class aircraft, Reist and Zingg [6] used exploratory aerodynamic shape optimization based on the RANS equations to develop a more efficient narrower BWB configuration and later corroborated these results in Ref. [7]. Some design challenges disproportionately affect smaller BWB aircraft. The centerbody packing problem is particularly restrictive, as typical airfoil thickness-to-chord ratios favor a single-deck centerbody design in which stowing conventionally positioned main landing gear without impinging on the cabin becomes difficult. However, the recently patented enabling technology of pivot-piston landing gear developed by DZYNE Technologies [18,30] solves this problem by way of hydraulically linked variable-length landing gear that can be positioned aft of the cabin in the tapering segment of the airfoil while

significantly reducing the aerodynamic force needed to achieve a given pitch acceleration during takeoff rotation. Thus, takeoff rotation ability can be decoupled from performance at other stages of flight, and in fact, a net performance benefit can be derived. For example, less lift-cancelling upward pitch control surface deflections are needed to hold the takeoff pitch attitude, so the landing gear weight penalty can be more than compensated by a reduction in the high-lift system weight at a constant takeoff field length (TOFL).

The primary goals of this work are: 1) to provide an updated and relatively credible assessment of the fuel-efficiency of regional-class BWB aircraft through a mixed-fidelity MDO framework that includes a high-fidelity RANS-based aerodynamics model, 2) to understand how the design features of the optimized aircraft arise as a consequence of the design requirements, and 3) to quantify the impact of some key design requirements on fuel efficiency. The 2019 study by Reist et al. [7] provides the starting point for this work, in which the optimization problem formulation is significantly expanded and refined, namely through higher design freedom and the consideration of additional critical takeoff and low-speed design requirements. The design mission over which block fuel burn is minimized is based on the capabilities of the Embraer E190-E2 regional jet; it consists of flying 104 passengers a distance of 3 100 nmi with an initial cruise altitude of 36 000 ft and a Mach number of 0.78. The optimizer is given significant freedom to determine the span and sweep of each major segment of the aircraft, in addition to several local twist angles, chord lengths, and cross-section shapes. Current technologies are favored even where proposed future technologies could be significantly beneficial. An assessment of the benefit of the BWB configuration alone is thus provided without introducing the guesswork associated with future technologies. Variable-length landing gear is considered the benchmark configuration, but a conventional landing gear arrangement is also analyzed.

An overview of the optimization framework is given in Section II, and the problem formulation is presented in Section III. Section IV discusses the optimized BWB aircraft and links several design features to the imposed design requirements. Section V shows design and performance sensitivities to the low-speed static margin and minimum control margin. Finally, Section VI gives the main conclusions of this work.

II. Mixed-Fidelity Multidisciplinary Design Optimization Framework

The tightly integrated nature of the BWB configuration implies strong design interdependencies [4], which must be carefully considered to produce a fuel-efficient aircraft. Hence, the design variables associated with several disciplines are simultaneously considered in the mixed-fidelity MDO problem solved in this work.

The computational framework called Jetstream is composed of the following five major components, which provide a mixed-fidelity MDO approach to aircraft development and performance assessment: 1) a geometry and grid parameterization module with integrated grid deformation [31], 2) a geometry control module [32], 3) a three-dimensional parallel implicit Newton-Krylov-Schur flow solver for the RANS equations coupled with the negative variant of the Spalart-Allmaras one-equation turbulence model [33], 4) several low-, medium-, and mixed-fidelity models mainly for non-aerodynamics disciplines [7], and 5) the Sparse Nonlinear Optimizer (SNOPT) local optimization algorithm [34] with flow-dependent gradient evaluation based on the discrete-adjoint method [35,36].

Previous versions of Jetstream have been applied to BWB-specific studies by Kuntawala et al. [16], Reist and Zingg [6], Reist et al. [7], Gray et al. [8], and Zingg et al. [9]. Jetstream has been cross-validated with an industrial aerodynamic shape optimization framework, showing excellent agreement over a range of challenging problems despite significant differences in the two frameworks [37]. The remainder of this section describes the components of Jetstream in greater detail and provides information about its application to this work.

A. Initial Geometry and Grid Definition and Parameterization with Integrated Grid Deformation

An initial geometry that reasonably approximates the anticipated optimal geometry and a high-quality multiblock structured computational grid must first be defined. The initial geometry used in this work is loosely based on the narrow-cabin BWB optimized by Reist et al. [7], and the 128-block half-model grid has a modified-O topology; a sample initial geometry and surface discretization are shown in Fig. 1. The grid shown is the last in a sequence of three increasingly fine grids used during optimization; as shown in Table 6 in the Appendix, it contains approximately 4.41 million nodes. The nodal density is slightly biased toward block interfaces to reduce the discretization error. Two versions of each grid are defined; one is conventional and models free-air flight while the other includes a ground plane with a boundary condition of tangential flow incoming at freestream speed to account for ground effect. On the finest grid used for cruise aerodynamic analysis during optimization, the average y^+ value is 0.69. This grid is associated with a nearly design-independent drag error of approximately 9.0% near the optima as calculated using Richardson extrapolation; therefore, the drag error can be largely accounted for in fuel burn calculations. Correction factors are also implemented for other aerodynamic coefficients, but as seen in the Appendix, their absolute value is smaller. The flow solutions remain free of significant wave drag and separation during grid refinement studies conducted on optimized geometries, suggesting that aerodynamic shape optimization, which is routinely performed on coarser grids than those used for rigorous flow analyses due in part to

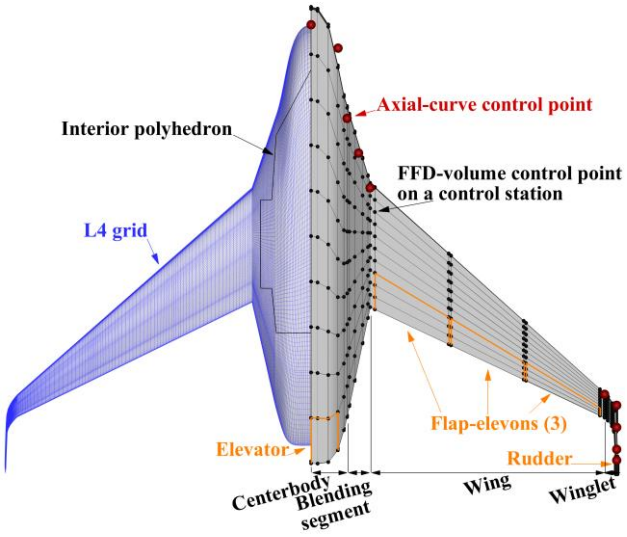

Fig. 1 Sample initial geometry, grid, axial-FFD system, interior polyhedron, and control surfaces.

computational resource limitations [6,7,11,20], can capture and exploit the essence of the modeled aerodynamic phenomena acceptably well. Nonetheless, it would be ideal to use a finer grid in future work involving fewer cases.

During an optimization iteration, a cubic B-spline parameterization of the grid is used to efficiently propagate aircraft surface deformations to the grid using a linear-elasticity-based grid deformation method [31,38]. An analytical B-spline surface parameterization of the block faces defining the aircraft surface is thus obtained, which, when perturbed, provides the boundary conditions for the grid deformation algorithm. Computational efficiency is ensured because the so-called control grid formed by the lattice of B-spline volume control points contains approximately 5-, 10-, or 20-times fewer nodes than the three computational grids used sequentially for optimization in this work. The fitting procedure used to define the B-spline volumes that parameterize the grid ensures that the nodal distribution in the control grid mimics that of the computational grid, which has higher node density in regions of high geometric curvature or where significant and detailed flow features readily exist, such as the boundary layer. The probability of maintaining high grid cell quality after grid deformation is thus increased.

B. Geometry Control

Geometry control is achieved through the free-form and axial deformation method [32], where the B-spline control points parameterizing the surface, as well as the control points of joined axial curves tied to the leading edge of the aircraft geometry, are embedded in free-form deformation (FFD) volumes. Embedding the B-spline-surface control points instead of the surface grid points has the advantage of maintaining an analytical representation of the

geometry throughout the optimization. The control points of the axial curve and the FFD volume are constrained to define common aircraft design parameters, namely span, sweep, dihedral, chord, twist, and cross-section shape.

In this work, four joined axial curves, which are B-spline curves of adequate control point density, are first fitted to the leading edge of the four main segments of the BWB aircraft, i.e., the centerbody, the blending segment, the wing, and the winglet. To avoid an excessively pointed nose, the centerbody axial curve is made parabolic and constrained to maintain a gently curving shape by defining any displacement of its middle control point to be a linear combination of the displacement of its two endpoints. The blending segment can be curved, but the two other axial curves, which control the wing and the winglet, are constrained to behave linearly. Four chordwise- and spanwise-cubic and vertically linear B-spline volumes, the FFD volumes, are then defined. They each encompass one axial curve and the corresponding geometry, resulting in a connected system of FFD volumes in which the aircraft surface control-grid points and axial curve control points are embedded.

The deformation of an axial curve controls the global dimensions of its corresponding FFD volume and the embedded geometry. The span, the sweep angle, and the wing dihedral angle are controlled through the spanwise stretching, the longitudinal shearing, and the constrained rotation about a longitudinal axis at the wing root, respectively. The FFD volume control points are grouped into several streamwise-aligned cross-sections, called control stations, that are fixed at a constant parametric location along an axial curve. Thus, the FFD volume control points provide local control over the twist angle, the chord length, and the cross-section shape. Rotating one such control station about the axial curve (the local origin) results in local twist control over the embedded surface control points, which translates to twist control over the geometry. Similarly, the uniform vertical and chordwise scaling of the control point locations about the axial curve provides chord-length control, and the displacement of the control points in the local normal direction, as determined by the local twist angle, results in cross-section shape control.

Trailing-edge control surfaces are modeled by rotating a given fraction of the aftmost FFD volume control points of a number of adjacent control stations through a specified deflection angle about a nearby hinge line [7]. Fig. 1 shows the axial curve and FFD volume control points, and the location and layout of the control surfaces. The pitch control surfaces on a half-model of the aircraft consist of one approximately 10%-chord elevator spanning the half-centerbody and three approximately 30%-chord flap-elevons each spanning one third of the wing. A rudder makes up approximately the aft 30% of the local winglet chord over the topmost 80% of the height. The elevator and flap-

elevons are considered saturated at 25 degrees, although tighter limits are imposed in this work to preserve controllability under critical low-speed conditions. The rudder can deflect by up to 30 degrees.

C. Flow Solver

Jetstream includes a three-dimensional parallel implicit Newton-Krylov-Schur flow solver for the RANS equations [33] closed with the negative variant [39] of the Spalart-Allmaras turbulence model [40]. Fully turbulent flow is assumed, and second-order centered difference summation-by-parts operators with simultaneous approximation terms are used for spatial discretization. The quadratic constitutive relations known as QCR2000 can be used for improved accuracy in the junction between the blending segment and the wing [41], which can be abrupt on some designs. Flow solutions are converged to a relative tolerance on the order of 10^{-10}. The flow solver has been validated at the Fifth AIAA Drag Prediction Workshop where the drag coefficient of the NASA Common Research Model was predicted within one count of the median across all participants [42,43].

D. Other Models

Multidisciplinary interactions are modeled with low-, medium-, and mixed-fidelity models. Weight calculations, propulsion system performance, and most contributions to excrescence, nacelle, and windmilling drag are captured with low-fidelity models, other aircraft mass properties are modeled with medium fidelity, and relevant flight mechanics quantities are modeled with mixed-fidelity physics-based equations.

1. Low-Fidelity Weight, Propulsion System, and Drag Augmentation Models

The MTOW is obtained through an iterative process involving the evaluation of component weights using an input MTOW value, the summation of those weights, and the verification of convergence against the input MTOW value [7]. No target MTOW is predetermined; rather, the aircraft and its components are sized as needed to satisfy the design requirements.

The low-fidelity cantilevered wing weight model of Torenbeek [44] is used. It depends on span, area, root thickness, sweep angle, and maximum zero fuel weight (MZFW). The loading term, MZFW, is scaled by the fraction of the lift carried by the wing to compensate for the load transferred to the centerbody. The blending segment and wing are combined into an equivalent trapezoidal wing of equal total area and span and of span-weighted average sweep angle. The winglet weight model is a function of its wetted area, and the explicit influence of winglet weight on wing weight is neglected in this work, as it is expected to have only a modest impact above

what is already captured by the correlative wing weight model. Fuel weights are estimated through fuel fractions considering warm-up, taxi and takeoff, climb, cruise, and landing [45]. An empirical relationship dependent on the initial cruise altitude of a mission is used for the climb fuel fraction. A cruise-climb profile at a constant Mach number and lift coefficient is assumed, so the cruise fuel fraction is calculated using a rearranged Breguet range equation corrected for a nonzero thrust angle. The cruise range is the total range discounted by the distance covered during a three-phase climb to cruising altitude at flight path angles of 4 degrees for the first 20 000 ft, 3 degrees for the subsequent 10 000 ft, and 2 degrees for the remainder of the climb. The descent fuel fraction is approximated through extending the cruise segment [44]; this approach is conservative but partially compensated for by the high engine thrust-specific fuel consumption (TSFC) at low thrust settings. In addition, a reserve fuel weight able to provide a 45-minute loiter and 100-nmi diversion both at a cruising altitude of 15 000 ft is considered. The sum of all fuel weights gives the value used for the maximum fuel weight (MFW). The sum of fuel weights from takeoff to landing (for the design mission) is the block fuel burn. The weight of unmodeled aircraft subsystems, termed fixed weights due to their negligible dependence on the considered design variables, is precalculated to be 24 000 lb using conceptual-level relations from Torenbeek [44], Roskam [46], and Raymer [45] and held constant [7,29]. The centerbody weight model developed by Bradley [47] is used. This model is sensitive to MTOW, pressurized cabin area, unpressurized centerbody area, and the taper ratio of the area aft of the cabin. This model was found to be in good agreement with a higher fidelity analysis for small BWB aircraft by Reist et al. [7]. Carbon-fiber-reinforced composites are used in the pressurized region, but proposed lightweight structural technologies such as PRSEUS [48,49] are excluded. A rubber engine model similar to that of Gur et al. [50] links the engine weight, the TSFC, the nacelle length and diameter, and the sea-level static (SLS) thrust to the ratio of the maximum cruise thrust to a reference value for the Pratt & Whitney PW1919G geared turbofan engine. The reference-engine dry weight is 4 800 lb, the cruise TSFC is 0.587 $lb_m/lb_f/h$, the engine length is 187.0 in, the inflow diameter is 81.0 in, and the SLS thrust is 20 860 lb [51,52]. The engine is sized based on the critical scenario among: 1) maintaining a top-of-climb rate of climb of 300 ft/min at cruise altitude [53], 2) maintaining a steady-climb flight path gradient of 2.4% (1.37°) after liftoff under OEI conditions [53], or 3) achieving a balanced TOFL of at most 5,410 ft under standard sea-level conditions, which is representative of the Embraer E190-E2. Section II.D.3 describes the flight mechanics models in more detail.

For increased accuracy in fuel weight calculations, low-fidelity estimates for excrescence and nacelle drag given by Torenbeek and Raymer [44,45] are added to the clean airframe drag obtained from CFD calculations, and windmilling drag [45] is added under OEI conditions. Excrescence drag is approximated as a 5% markup to parasitic drag, which is itself approximated using a RANS-validated form factor of 1.20 and the Mach-number-corrected Prandtl-Schlichting relation for the skin friction coefficient in turbulent flow [7]. Nacelles are excluded from the CFD grid for robustness under large geometric changes, and their parasitic drag is approximated with a form factor dependent upon the nacelle-diameter-to-engine-length ratio. Windmilling drag accounts for both the internal and external drag of the inoperative engine, and it is proportional to the frontal area of the fan.

2. Medium-Fidelity Mass-Properties Models

Other mass properties, namely the CG and pitching mass moment of inertia about the main landing gear, are calculated based on the grid and a few simplifying assumptions. The structural mass of the centerbody, blending segment, wing, and winglet is assumed to be homogeneously distributed within the shell of the airframe. The fuel weight is assumed to act through the wing volume centroid, the fixed weights are assumed to act through the shell centroid of the centerbody, and the payload weight is assumed to act at the volume centroid of the interior polyhedron shown in Fig. 1, which is extruded 7.6 ft deep and contains the flight deck, the cabin, and the cargo holds. The two aft-centerbody-mounted engines are treated as fixed point-masses whose position is updated between optimization warm-starts as described in Section III.E, thus preventing the optimizer from moving the thrust line downward unrealistically by creating a u-shaped dip in the centerbody trailing edge at the engine attachment point. Their exhaust is ultimately longitudinally positioned approximately one nacelle diameter ahead of the centerline trailing edge, and their centerlines are vertically positioned one-half nacelle diameter above the fixed nose and laterally separated by two nacelle diameters. The JetZero BWB aircraft has similar engine positioning, and it does not ingest the boundary layer; rather, external diffusion, bump diverters, and ducted diverters redirect the boundary layer under the engines and reintroduce it into the flow along the vertices of the nozzle-airframe junction [18]. Interference effects, which may be particularly strong on narrow-centerbody designs, are assumed to be manageable during later design stages through, for example, engine canting and winglet and rudder resizing.

3. Mixed-Fidelity Flight-Mechanics Models

The flight-mechanics models considered in this work combine data from the other models. The nature of the considered models is first discussed here; more specific details are given in Table 1 and Section III.C. Trim, the top-of-climb rate of climb, and the initial pitch acceleration produced by the pitch control surfaces during takeoff rotation are calculated through equilibrium while considering aerodynamics, engine thrust, and aircraft weight, as appropriate. The aerodynamic derivatives required for the calculation of the static margin, namely the slopes of the lift and pitching moment curves, are approximated through first-order forward finite differences with respect to the angle of attack ($\Delta\alpha = 0.1$ deg), where the CG determines the moment summation point. Mixed-fidelity models for the TOFL, the takeoff decision speed, V_1, the all-engines-operational (AEO) and OEI steady-climb speeds, $V_{\mathrm{SC}_{\mathrm{AEO}}}$ and $V_{\mathrm{SC}_{\mathrm{OEI}}}$, the AEO and OEI steady-climb flight path angles, $\gamma_{\mathrm{SC}_{\mathrm{AEO}}}$ and $\gamma_{\mathrm{SC}_{\mathrm{OEI}}}$, and the level-flight power-off (reference) stall speed, V_s, are implemented. These quantities depend on weight, engine performance, and on-ground and low-speed aerodynamics in addition to the critical engine-failure speed, V_{EF}, the takeoff rotation speed, V_{R}, the AEO and OEI liftoff speeds, $V_{\mathrm{LOF}_{\mathrm{AEO}}}$ and $V_{\mathrm{LOF}_{\mathrm{OEI}}}$, and the time airborne to reach the 35-ft takeoff screen height under AEO or OEI conditions. The TOFL is calculated as per Part 25 of the Federal Air Regulations [53] through integrated equations of motion. It is the greatest among the AEO or OEI accelerate-stop or accelerate-go distances.

E. Gradient Evaluation and Optimization

The SNOPT gradient-based local optimization algorithm [34] is used, as it can efficiently solve large scale nonlinear constrained optimization problems. In this work, an optimization problem is considered converged when 1) each scaled constraint is satisfied to an absolute tolerance of at least 10^{-6}, and 2) the SNOPT optimality metric, which measures the satisfaction of the first order Karush-Kuhn-Tucker optimality conditions, has been reduced to a value on the order of 10^{-5} (typically representing a drop of 1 to 2 orders of magnitude), and at least 10 successive SNOPT major iterations have produced objective function variations in at most the fifth significant figure.

Accurate gradients are required to converge the optimization problem. Due to the large number of design variables (see Section III.D) relative to the number of required flow-dependent gradients, the latter are evaluated using the discrete-adjoint method [35,36], with the necessary partial derivatives obtained via the complex-step method or analytical differentiation, as appropriate [31,36]. The adjoint system is solved to a tight tolerance of 10^{-8}

using a simplified and flexible version of the generalized conjugate residual with orthogonalization and truncation (GCROT) algorithm [55].

III. Optimization Problem Formulation

This section presents and justifies the formulation of the mixed-fidelity MDO problem solved in this work, which is constructed using the elements described in section II.

A. Objective Function and Mission

An industry-relevant, system-level objective function with the following characteristics is sought: 1) low absolute modeling error for accurate performance evaluation, 2) low design- or configuration-specific modeling error for accurate relative performance evaluation, 3) a bias toward environmental performance to mirror the current focus on sustainable aviation, and 4) low variability across missions to reduce or avoid the need to analyze and average performance over many different missions. Chau and Zingg [11–13], and Zingg et al. [9] minimized block fuel burn in RANS-based comparative studies of unconventional and CTW aircraft. An example of a performance metric biased farther toward profitability is direct operating costs, and one biased farther toward environmental performance is climate change impact. Block fuel burn is an important part of both metrics, but the latter has very high modeling error and strong dependence on highly variable mission parameters such as cloud cover [56]. Therefore, design-mission block fuel burn is selected as a performance metric in this work.

A maximum-payload and a maximum-range mission define the MTOW-limited portion of a classical payload-range diagram used for transport aircraft sizing. The MTOW-limited design mission with a full passenger payload lies somewhere between these two points. It is used for performance analysis and sizing in this work since the main goals are not dependent on matching the exact capabilities of a reference aircraft. The design mission of the Embraer E190-E2 best-in-class regional jet is used as a reference [54]. It consists of flying 104 passengers a distance of 3 100 nmi with an initial cruise altitude of 36 000 ft and a Mach number of 0.78. The Reynolds number based on a good approximation of the mean aerodynamic chord (MAC) of the optimal design, 42.4 ft, is 76.55 million. Diversion and loiter mission segments consist of flying an additional 100 nmi and loitering for 45 min, both at an altitude of 15 000 ft and a Mach number of 0.50; design-mission cruise data is reused to simplify this calculation.

BWB aircraft typically reach an optimal balance between zero-lift drag and lift-dependent drag at higher cruise altitudes than CTW aircraft due to their lower wing loading [1,6,9,57]. However, nitrogen oxides in aircraft exhaust

have a greater atmospheric impact at higher altitudes [58], and the weight of the noncylindrical pressure vessel gets increasingly high and uncertain. It is therefore useful to optimize BWB aircraft for a currently typical cruise altitude to investigate whether the configuration remains particularly efficient. A narrow cabin can lead to a lower surface area and a better balance in the components of drag at relatively low cruise altitudes [7,57].

B. Technology Levels

A BWB aircraft is several years away from being built [18], so it can be tempting to outfit the aircraft with compatible future technologies to assess its potential. For example, low-nitrogen-oxide combustors could open the possibility of increasing cruise altitudes and thus BWB fuel efficiency while keeping climate change impact low [59], sustainable aviation fuels such as hydrogen are compatible with the often larger internal volume of a BWB aircraft [60], PRSEUS technology could enable a low-weight noncylindrical pressure vessel [48,49], and boundary-layer-ingesting engines and distributed propulsors can ingest a significant portion of the centerbody boundary layer. However, including such models in the optimization would require significant speculation that degrades the credibility of the output block fuel burn estimate. For that reason, and to eventually quantify the performance gap between current CTW aircraft and a BWB that could be built in the next few years, this work focuses on BWB aircraft outfitted with current technologies. Thus, current materials are assumed for the airframe, the engines are modeled after the existing Pratt & Whitney PW1919G engine, folding wingtips can be used, kerosene-based jet fuel is used, and fully turbulent flow is assumed. The variable-length landing gear discussed in Section I is considered, but so is a conventional landing gear arrangement.

C. Design Requirements and Analysis Points

The design requirements summarized in Table 1 are assumed to be particularly critical to the determination of the primary design features and the accurate calculation of the design-mission block fuel burn. Thus, the aircraft must be analyzed at the start of cruise, on the ground at the minimum control speed, $V_{\mathrm{MC_G}}$, and at the takeoff rotation speed, V_{R}, and in low-speed flight at sea level outside of ground effect. The rotation analysis is excluded when variable-length landing gear is considered. These analysis points and the design requirements are further discussed next.

Table 1 Summary of performance-based design requirements and other nonlinear design constraints

Constraint	Description
Start-of-cruise trim	The sums of vertical forces and of pitching moments must vanish, respectively, while considering aerodynamics, thrust, and weight, but no control surface deflections.
Top-of-climb rate of climb	The excess thrust at the top of climb must give a rate of climb of at least 300 ft/min.
OEI-$V_{\mathrm{MC_G}}$ directional trim	The rudders must be able to trim the unbalanced thrust at a 97-kt $V_{\mathrm{MC_G}}$.
Takeoff rotation capability	When variable-length landing gear is not used, an initial pitch acceleration of 3 deg/s^2 must be produced by deflecting the pitch control surfaces at V_{R}.
Takeoff field length	A TOFL of at most 5 410 ft [54] is imposed while considering accelerate-stop and accelerate-go conditions under both AEO and OEI conditions.
Critical steady-climb flight path angle	An OEI steady flight path gradient of 2.4% (1.37°) must be achievable after liftoff.
Safety margin to stall speed	$V_{\mathrm{LOF_{AEO}}}$, $V_{\mathrm{LOF_{OEI}}}$, $V_{\mathrm{SC_{AEO}}}$, and $V_{\mathrm{SC_{OEI}}}$ must exceed $1.13V_s$ [53].
Engine failure response	There must be a two second margin between V_{EF} and V_1 [53].
Rotation speed	V_{R} must exceed V_1.
Rotation time	As a static proxy to the dynamic maneuver, the time between V_{R} and $V_{\mathrm{LOF_{OEI}}}$ or $V_{\mathrm{LOF_{AEO}}}$ must be at least 2.5 seconds.
Critical low-speed trim	The sums of vertical forces and of pitching moments must vanish, respectively, while considering aerodynamics, thrust, and weight during a 132-kt approach; flap-elevon deflections are allowed, but no slats are considered in this work.
Critical low-speed static margin	A relaxed static margin of -4% MAC_0 is imposed under critical CG (aftmost), weight (MTOW; conservatively), and thrust (zero) conditions during a 132-kt approach.
Interior polyhedron inclusion	The flight-deck and cabin must reside within the centerbody, and the cargo hold must reside within the centerbody and/or the blending segment.
Wing volume	57.6% of the wing volume less a 5-ft wingtip margin must exceed the fuel volume.
Wingtip strike	Wingtip ground-strike protection must be guaranteed up to a simultaneous 9° pitch attitude and 9.5° roll attitude both about a conventionally positioned main gear wheel.
Ground clearance	A ground clearance of at least 3 ft must be maintained when all wheels are on the ground and variable-length landing gear is unactuated (flat cabin).
Centerbody rounded nose	For flight-deck positioning and transonic shock and separation mitigation during a sideslip, the initial rounded centerbody nose shape must be maintained through interpolating the centerbody chord perturbations and limiting the foremost top and bottom section-shape design variables to 80% of their initial value.

1. Cruise Design Requirements

The aircraft lift and pitching moment must be trimmed at the start-of-cruise analysis point, whose conditions are as described in Section III.A, with the corresponding weight, CG, and thrust. The pitch control surfaces are not free to help trim the aircraft, and the top-of-climb rate of climb, which must exceed 300 ft/min, is calculated based on data from this analysis point. The cruise static margin is not constrained because the low-speed equivalent is critical.

2. Takeoff Design Requirements

As a static proxy for the dynamic on-ground minimum control speed requirement that helps size and position the vertical surfaces and rudders, the aircraft must achieve directional trim at $V_{\mathrm{MC_G}}$ = 97 kt under OEI conditions. The low speed likely makes this design requirement more critical than crosswind flight [7]. The nose landing gear is conservatively assumed to be unloaded, so it produces no lateral force opposing the engine yawing moment. As per Reist et al. [7], large winglets perform similarly to centerbody-mounted fins, so the latter configuration is not studied here. Half-model grids reduce computational cost and are used despite the small asymmetry in rudder effectiveness.

Achieving takeoff rotation using pivot-piston variable-length landing gear requires an aerodynamic force similar to that required to pitch about the CG [18,30], which is significantly smaller than that required to pitch about conventional main landing gear. A constraint on the achievability of takeoff rotation is assumed redundant if variable-length landing gear is considered. This assumption has been validated after optimization. Conversely, when conventional landing gear is used, takeoff rotation is considered achievable if the pitch control surfaces can cause an initial pitch acceleration of 3 deg/s^2 about the main landing gear at V_{R}, which is determined by the TOFL model. The elevator and flap-elevons are limited to 80% and 50% of their 25-degree deflection limit, respectively, to maintain a controllability margin. The conventional main landing gear is longitudinally positioned where a line emanating from a point 1%-MAC$_0$ behind the aftmost CG and tilted rearward by 10° from the vertical intersects the plane of the main landing gear axles; MAC$_0$ is the MAC of the initial geometry, which is made to be a good approximation of the optimal geometry. The rotation constraint is analyzed in ground effect with the worst-case combination of weight and CG. To account for possible variations in payload distribution, the MTOW, MZFW, and MFW CGs are conservatively perturbed forward by 2% MAC$_0$ and the operating empty weight (OEW) CG is conservatively perturbed forward by 3.5%-MAC$_0$. Full SLS thrust is used, as the engines produce a nose-down pitching moment.

The engines are sized based on the critical operational scenario, as described in Section II.D.1. Safety regulations require that the takeoff safety speed, V_2, exceed V_s by a factor of at least 1.13, in particular under critical (OEI) conditions [53]. Further constraining $V_{\mathrm{LOF_{AEO}}}$ and $V_{\mathrm{LOF_{OEI}}}$ as such is slightly conservative, as the aircraft typically accelerates from liftoff to the 35-ft screen height, but this approach avoids considering the nontrivial critical deviation from an optimal takeoff flight path. Instead, a constant airborne-segment lift coefficient equal to that required at liftoff is assumed [61]. However, the resulting speed and flight path angle measured at the screen height may seldom occur in practice and may be unsustainable especially without retrimming, so the initial-climb

constraints are imposed on the steady-climb speeds, $V_{\mathrm{SC_{AEO}}}$ and $V_{\mathrm{SC_{OEI}}}$, and flight path angles, $\gamma_{\mathrm{SC_{AEO}}}$ and $\gamma_{\mathrm{SC_{OEI}}}$, at the optimizer-selected lift coefficient; OEI conditions are critical. Moreover, the minimum allowable time elapsed between V_{R} and $V_{\mathrm{LOF_{AEO}}}$ or $V_{\mathrm{LOF_{OEI}}}$ is 2.5 seconds, which is a simplified representation of the dynamic takeoff rotation maneuver based on a constant 3-deg/s^2 pitch acceleration and an approximate liftoff angle of attack of 10°. Finally, V_1, which is the speed achieved two seconds after V_{EF}, must be less than V_{R}.

3. Low-Speed-Flight Design Requirements

The static margin of the trimmed aircraft is calculated as described in Section II.D.3, and it must be kept above -4% MAC_0 under the tested critical conditions of 1) the aftmost CG, 2) the heaviest weight (MTOW), 3) the lowest reasonable speed (132 kt, which approximates 1.13 times V_{s}), and 4) zero thrust. The first condition reduces the aircraft stability directly, the second and the third induce a high angle of attack (and thus a high nose-up pitching moment given that the aircraft is statically unstable), which, like the fourth, induces high downward pitch control surface deflections for those control surfaces that are positioned on wing segments with a center of pressure lying behind the CG. As discussed in Section IV.B.4, downward control surface deflections cause a significant forward movement of the local aerodynamic center, thus destabilizing the aircraft. Indeed, the benchmark optimized aircraft is allowed to be slightly statically unstable to improve performance [4,7]. Implicit in this assumption is the certifiability of stability augmentation software before BWB aircraft enter the market; however, Section V discusses the implications of requiring a positive static margin. The pitch control surface deflection limits are the same discussed in Section III.C.2.

4. Sizing Design Requirements

The interior polyhedron must be enclosed within the outer mold line of the aircraft. Specifically, the flight deck and cabin must reside within the centerbody, and the cargo holds must lie within the centerbody and/or the blending segment to keep the conceptual-level area-based centerbody weight model within its range of validity [47].

The fuel volume corresponding to the MFW must fit within the usable fraction of the wing outer mold line. As in Ref. [7], the wing box is assumed to lie between 20% and 70% of the local wing chord. When also accounting for the usable volume within the wing box, 57.6% of the wing outer mold line volume is found to be usable to store fuel. However, a 5-ft margin from the wingtip is also considered due to lightning strike requirements.

The wingtips must be protected from ground strikes under critical conditions representative of a momentarily destabilized final approach. A simultaneous pitch and roll attitude of 9° and 9.5°, respectively, is considered, with rotations being calculated about a conventionally positioned main landing gear wheel. The exact position of variable-length landing gear is assumed to insignificantly change the impact of this constraint, so no adjustment is made in corresponding cases. The conventional main landing gear is laterally positioned 2-ft outboard of the cargo holds. Its longitudinal position is described in Section III.C.2. This constraint is almost always critical when compared to a centerbody tail-strike constraint for the designs studied here, as a 3-ft ground clearance margin is also imposed when variable-length landing gear is unactuated. The wing dihedral angle can be used to satisfy the wingtip-strike constraint by increasing the wingspan and sweep freedom, but this parameter is capped at 4° to help prevent unconsidered Dutch-roll underdamping.

D. Design Variables and Other Constraints

An appropriate quantity of design variables of various types is selected to avoid 1) unrealized potential performance due to implicitly overconstrained problems, and 2) manufacturability issues [62], nearly redundant design variables [32], and slow or stalled optimizer convergence [63]. Table 2 summarizes the design variables and their bounds. Among the geometric design variables, the span and sweep angle of each aircraft segment are free, except a small lower bound on winglet span (height) is used to prevent its collapse in some cases, and the dihedral angle of the wing can vary as discussed in Section III.C.4.

The high-fidelity aerodynamics model is sensitive to the exact shape of the aircraft outer mold line, so a large majority of the design variables control the cross-section shapes. Twenty-two FFD control points: eleven on top and eleven on the bottom, are aligned among eleven effective control stations over the half-span of the aircraft. The centerbody, blending segment, and main wing each have three (one at the root and two in the middle), and the winglet has two (one at the root and one at the tip). The first and the last top-bottom pairs of FFD control points at each control station are constrained to move in an equal-but-opposite manner to inhibit the use of cross-section-shape design variables as makeshift twist design variables through shearing. Due to the absence of a structural model, the lower bound on section thickness-to-chord ratios for the main wing and winglet is 80% of the initial value, which corresponds to an SC(2)-0012 airfoil. This limitation avoids excessively thin sections by keeping the wing root and tip at least 9.6% and 8.0% thick, respectively.

Table 2 Summary of effective design variables and select bounds and constraints

Design variable type	Quantity				Select bounds and constraints
	Cruise	OEI-V_{MC_G}	Low speed	Rotation*	
Angle of attack	1		1		Cruise deck angle between 0° and 3°
Elevator deflection			1	1	±20.0°
Flap-elevon deflection			3	3	±12.5°
Rudder deflection		1			±30.0°
Twist angle		11			
Cross-section shape		220			Wing and winglet local $t/c \leq 0.8(t/c)_0$
Chord length†		5			Centerbody chord perturbation interpolated between start and end points; blending segment, wing, and winglet chords linearly interpolated; wing tip ≥ 5 ft; winglet tip ≥ 3 ft
Segment span† (incl. winglet height)		4			Centerbody span ≥ cabin width; Middle centerbody and blending segment axial curve control point spanwise coordinate perturbation interpolated between endpoints.
Segment sweep†		4			
Wing dihedral		1			Between 0° and 4°
Interior polyhedron perturbation		3			Polyhedron nose at most 11 ft from aircraft nose
OEW CG perturbation		1			±5% MAC_0
Takeoff field length variables		6			V_1 (which is ≥ V_{EF}) ≤ V_R, $V_R \leq V_{LOF_{OEI}}$ and $V_{LOF_{AEO}}$
Engine scaling		1			
Thrust-line angle		1			±2°
Total		268			

* Excluded if variable-length landing gear is considered.
† These variables are constrained by the interior polyhedron inclusion requirement.

Each control station can independently twist the embedded aircraft geometry. The twist of the winglet is linearly interpolated between its endpoints to improve grid deformation robustness at little cost to performance.

The chord length of control stations at the edge of the centerbody, blending segment, wing, and winglet is free. The chord perturbations are linearly interpolated at the control stations in the interior of the centerbody to help avoid a wedge-shaped nose that may be susceptible to transonic separation or compressibility effects under slight sideslip. The wing tapers linearly for conformity to the wing weight model [44], and so do the blending segment and winglet to improve grid deformation robustness at an assumed small cost to performance. The wing and winglet tip chords are kept above 5 ft and 3 ft, respectively, for structural reasons and to help accommodate rudder hardware.

Other design variables influence an aspect of the design unrelated to outer-mold-line geometry. The angle of attack is free at cruise and at the low-speed-flight analysis point, where the pitch control surfaces are free. They are also free at the takeoff rotation analysis point, and the rudders are free at the OEI-V_{MC_G} analysis point. Six design

variables help satisfy the takeoff and initial-climb constraints; these are V_{EF}, V_{R}, $V_{\mathrm{LOF_{AEO}}}$, $V_{\mathrm{LOF_{OEI}}}$, and the airborne times required to reach the 35-ft takeoff screen height under AEO and OEI conditions. The engine scaling factor is a design variable and so is the thrust-line angle, which is limited to ±2° to help efficiently orient the (fixed-position) engine relative to the airflow without causing excessive cyclical blade loading. The interior polyhedron is optimally positioned through a longitudinal, a vertical, and a pitch angle design variable; however, the deck angle must lie between 0° and 3° at the cruise analysis point, and the frontmost point of the polyhedron must lie between 0 ft and 11 ft from the tip of the nose to help maintain good pilot visibility. Lastly, the calculated OEW CG can be perturbed fore or aft by 5% MAC_0 to account for modeling uncertainty and strategic systems layout decisions.

E. Optimization Problem Solution Strategy

The multi-stage strategy shown algorithmically in Fig. 2 is used to solve the mixed-fidelity MDO problem efficiently and effectively through grid sequencing and parameter estimation. The optimization is initially undertaken on the coarse L_0 grids (see the Appendix) with respect to the twist, cross-section-shape, and some non-geometric design variables (interior polyhedron perturbation, OEW CG perturbation, and thrust-line angle), and the cruise trim and sizing constraints are enforced. Low initial turnaround times allow for quick identification and correction of issues with the problem setup. Once an optimal solution is found, the discretization-error correction factors discussed in Section II.A are computed and the optimization is warm-started on the L_2 grid with all design variables and constraints. The other fixed parameters discussed below are then recomputed before launching another warm-started optimization on the same grid. After convergence, the discretization-error correction factors are recomputed; these final values are reported in Table 6 in the Appendix. The cruise grid is then refined one last time to the L_4 level, the L_3 grid is used for the low-speed-flight analysis point, and the L_2 grid is reused for the OEI-$V_{\mathrm{MC_G}}$ and rotation (when considered) analysis points. Flow solution results thus correspond with the desired constraint evaluation accuracy; namely, the finest grid used for cruise performance analysis increases the accuracy of the calculation of the relative contributions of zero-lift and lift-dependent drag.

Select parameters are treated as fixed during optimization and updated between warm-starts as more information on the optimal design becomes available. Namely, the takeoff constraints are not sufficiently sensitive to the costly-to-compute liftoff angle of attack, zero-lift drag coefficient, and induced-drag factor $1/\pi e$ AR to justify updating these quantities during optimization. The maximum lift coefficient used is based on a fine-grid estimate produced

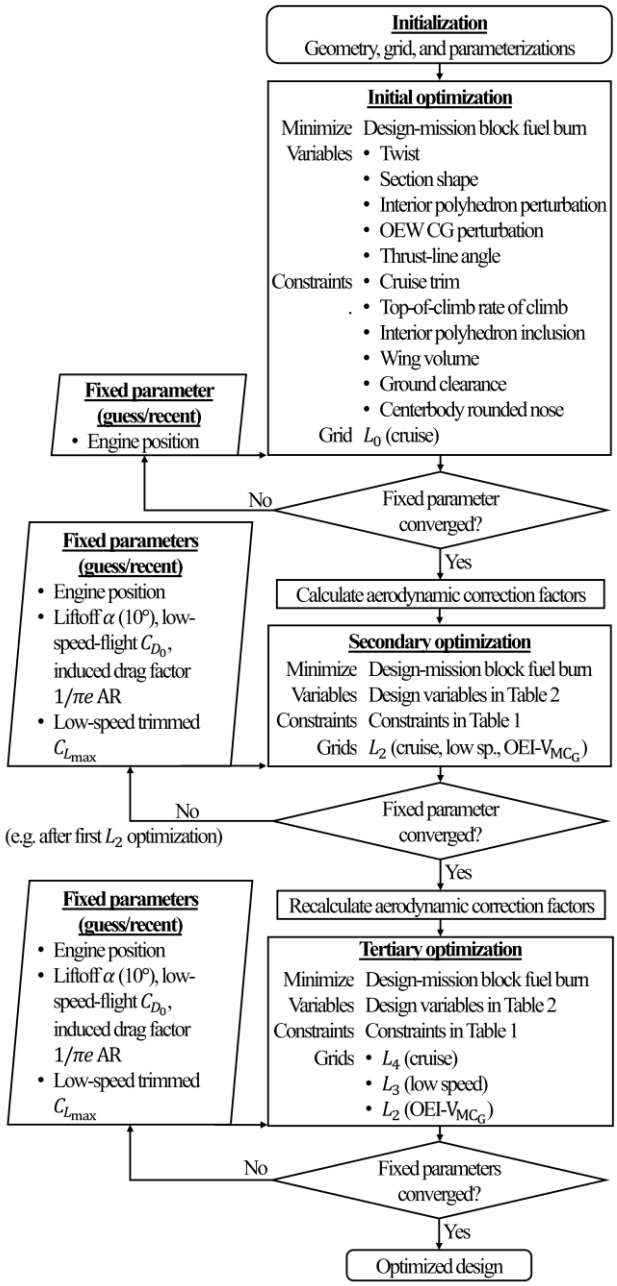

Fig. 2 Optimization flowchart for the benchmark case; other cases are warm-started after loop 1.

using the pitch control surface deflections found to be optimal at the low-speed-flight analysis point. As shown in Fig. 3, the value of $C_{L_{\max}}$ increases with increasing nodal density; Richardson extrapolation would provide a more accurate value, but it is not used in order to remain conservative. Finally, the longitudinal and vertical position of the engines is treated as fixed during optimization to avoid the problem exploitation discussed in Section II.D.2.

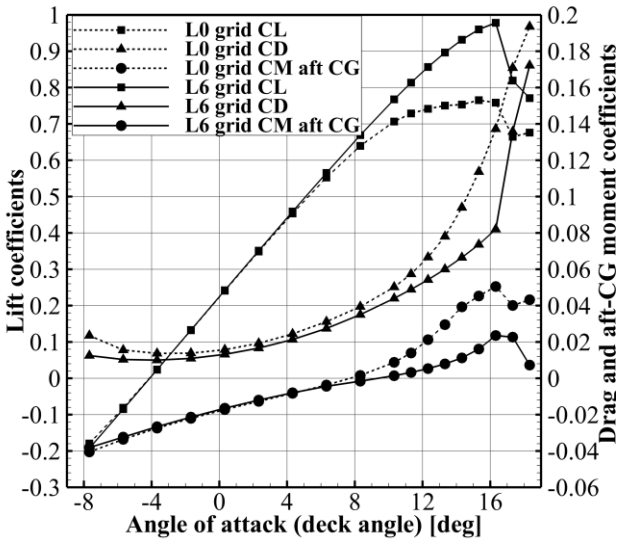

Fig. 3 Lift-, drag-, and moment-coefficient curves for the optimized benchmark design as trimmed for low-speed flight.

IV. Optimal Design and Performance

The design and performance of the optimized benchmark aircraft is discussed in this section along with the solution to six complementary optimization problems that demonstrate the impact of the primary design requirements and elements of design freedom. In case 1, only the cruise and sizing design requirements are considered, so the combined effect of all takeoff and low-speed design requirements is quantified. More precise insight is gained on several design requirements in cases 2 through 4, where a select few are removed from the optimization problem individually or as a small group. In case 2, the OEI-$V_{\mathrm{MC_G}}$ directional-trim constraint is not imposed; in case 3, the TOFL and initial-climb constraints are removed; and in case 4, the low-speed static margin constraint is not imposed. In case 5, the variable-length landing gear is replaced by a conventional arrangement, and in case 6, some geometric freedom is removed from the centerbody and blending segment by linearly interpolating the twist and cross-section shapes between the endpoints, thus highlighting the purpose of nonlinear spanwise variations in these parameters in the benchmark case. The characteristics and performance of each optimized aircraft are contained in Table 3, and Table 4 shows which inequality constraints are active at the optimum.

A. Overview of the Optimized Benchmark Aircraft

Top and front views of the optimized benchmark aircraft are shown in Fig. 4 along with the pressure coefficient contours and chordwise distributions, the spanwise lift distributions, the center of pressure and aerodynamic center locations at the cruise analysis point, and the CGs for the MTOW, MZFW, MFW, and OEW loading conditions. Shocks are eliminated on all optimal designs, contributing to a cruise lift-to-drag ratio of 21.7, which is close to the value of 21.6 predicted by DZYNE Technologies for a similarly capable aircraft [18]. The cruise lift distribution is nearly elliptical, although this is not an exact target due in part to the winglet and the need to trim the pitch axis without a tail. Compared to a related case solved by Reist et al. [7], which includes a rotation constraint and conventional landing gear but significantly lower design freedom (among other less relevant differences), the centerbody lift distribution is fuller despite the increased number of particularly punitive design requirements in this work. This observation also applies to case 5, which includes the rotation constraint and conventional landing gear and produces a similar cruise lift-to-drag ratio of 21.8. Thus, high design freedom (including higher pitch control surface deflections) is critical in realizing the aerodynamic potential of the tightly integrated BWB configuration. Furthermore, case 6 highlights the importance of high geometric freedom alone; the cruise lift-to-drag ratio is lowered to 21.1 through interpolating the centerbody twist and section shape design variables.

The centerbody (excluding the blending segment) carries 15.1% of the lift at the cruise analysis point, the (invariable) 7.6-ft blending segment root is thick, and the 105.8-ft bending span is laterally offset by the centerbody and blending segment. Each design feature contributes to producing the comparatively high 132.2-ft wingspan at low weight, which helps generate low induced drag. However, this wingspan exceeds the 118-ft limit for the code-C airport gates often used for regional aircraft; hence folding wingtips may be needed.

The OEW of the optimized benchmark aircraft is 65 170 lb, which is 10.4% lighter than that of the Embraer E190-E2 [54]. The E190-E2 weight breakdown estimate given by Chau and Zingg suggests that the lightweight structure of the BWB is enabled due to the lack of an empennage and lighter wings due to lower wing loads [11].

The competing S&C constraints pressure the optimizer to keep each CG mutually close; every CG falls within a range of just 2.20 ft (5.2% MAC_0). This unanticipatedly contributes toward low trim drag variations throughout the entire flight. The low-speed static margin constraint is calculated using the aftmost CG, but it benefits from nose-heaviness. Therefore, the optimizer is pressured to move the aftmost CG forward, and it fully uses the CG perturbation design variable to help achieve this goal. The cruise static margin is positive and equal to 1.78% MAC_0

even when perturbed to consider the aftmost CG. However, trim drag increases at cruise if the cruise CG, which is 0.2%-MAC_0 more forward than the CG at MTOW, is so far forward that the equilibrium point for zero trim drag is exceeded. One design variable that helps limit the forward movement of the cruise CG without affecting the position of the aftmost CG, which corresponds to the MFW loading condition and therefore considers no payload, is the longitudinal perturbation of the interior polyhedron. Indeed, this variable is used at least in part to shift the payload CG aft, as seen in Table 4.

In Refs. [6,7], the optimizer exploited a transonic compressible flow effect to push the wing aerodynamic centers aft to impractically help satisfy a cruise static margin constraint. The small dent observed in the upper surface of the wing near the wingtip is absent in the optimized geometries obtained in this work, as it does not help satisfy the more critical low-speed static margin constraint.

The trim problem is underdetermined because five design variables that are specific to the low-speed-flight analysis point – three flap-elevon deflections, one elevator deflection, and one angle of attack – are used to satisfy at most three conditions: lift and pitch trim and the active static margin constraint. The optimizer first attempts to resolve the redundancy by maximizing the static margin (an active inequality constraint) with respect to the five aforementioned analysis-point-specific design variables while satisfying the trim equality constraints. Indeed, performance at other stages of flight would be sacrificed by prioritizing outer-mold-line design variables instead of analysis-point-specific design variables. The former design variables are leveraged to satisfy the low-speed-flight constraints only if the latter are first optimally used, and in such a case, the outer-mold-line design variables used are selected in the order that minimizes the impact on the objective function. For example, the optimized benchmark design has a 7.9% longer centerbody than the optimized geometry from case 1, as this design feature is particularly effective at increasing the effectiveness of the downward-saturated elevator at the low-speed-flight analysis point. It appears that the associated weight and friction drag penalties are worthwhile. The elevator, with its long lever arm, is particularly effective at satisfying the trim constraints, and since the optimizer chooses to increase its effectiveness despite the middle and outboard elevons being unsaturated, the latter are inferred to be relatively destabilizing; this fact is explicit in Fig. 5. Moreover, the optimizer can leverage the OEW CG perturbation design variable to lengthen the centerbody without impacting the CG, but only within the allowed perturbation range, which is entirely used.

Table 3 Characteristics and performance of the optimized aircraft

Measurement Excludes →	Benchmark	Case 1 Off-design	Case 2 OEI-V_{MC_G}	Case 3 Takeoff	Case 4 LS K_n	Case 5 Var. gear	Case 6 Geo. free.
Aspect ratio	6.56	6.48	6.99	6.64	6.51	7.32	6.57
Wetted aspect ratio	2.77	2.78	3.02	2.83	2.77	3.13	2.84
Planform area [ft^2]	2 664	2 521	2 672	2 639	2 636	3 023	2 885
Wetted area [ft^2]	6 313	5 865	6 184	6 202	6 202	7 074	6 669
Span [ft]	132.2	127.8	136.6	132.4	131.0	148.8	137.7
Wing LE sweep [deg]	31.9	35.6	30.6	31.7	33.7	35.7	33.5
Winglet LE sweep [deg]	44.3	60.0	60.6	48.1	46.6	32.2	44.8
MTOW [lb]	111 900	108 200	111 400	109 400	111 500	118 500	113 900
MZFW [lb]	88 050	85 140	87 780	85 760	88 020	93 520	89 020
OEW [lb] (incl. fixed weights)	65 170	62 260	64 900	62 880	65 140	70 640	66 140
Centerbody [lb]	22 170	21 790	22 130	22 030	22 150	23 730	23 750
Wings [lb]	10 160	9 670	10 270	9 790	10 090	12 790	10 080
Winglets [lb]	433	244	191	343	414	434	350
Engines [lb/engine]	4 200	3 280	4 160	3 360	4 240	4 850	3 970
MFW [lb]	23 810	23 080	23 640	23 680	23 460	25 010	24 830
Block fuel burn [lb/pax/nmi]	0.0619	0.0601	0.0615	0.0616	0.0611	0.0651	0.0646
OEW forward CG pert. [% MAC_0]	5.00	-5.00	5.00	5.00	1.12	5.00	5.00
Max. SLS thrust [lb/engine]	17 820	13 310	17 610	13 700	18 050	21 100	16 710
Max. cruise thrust [lb/engine]	3 720	2 780	3 680	2 860	3 770	4 400	3 490
Thrust-line angle [deg]	-0.5	1.1	0.1	-0.1	0.1	-2.0	-0.9
Cruise TSFC [$lb_m/lb_f/h$]	0.591	0.598	0.591	0.598	0.591	0.587	0.593
Cruise deck angle [deg]	3.0	2.7	3.0	3.0	3.0	1.6	3.0
Cruise L/D	21.7	21.9	21.8	21.5	22.0	21.8	21.1
Cruise C_L	0.203	0.207	0.201	0.200	0.204	0.189	0.191
Cruise C_D [counts]	93.5	94.6	92.4	93.3	92.9	87.0	90.5
Cruise drag [lb]	5 070	4 860	5 030	5 010	4 980	5 350	5 310
Cruise K_n* [% MAC_0]	1.78	-3.78	1.61	1.74	-1.33	1.67	3.60
Cruise centerbody lift fraction [%]	15.1	15.1	15.1	15.2	14.8	14.2	18.7
Low-speed (LS) deck angle [deg]	8.9	N/A	9.0	8.9	7.6	6.4	9.5
LS C_L	0.708	N/A	0.703	0.699	0.713	0.661	0.665
LS centerbody lift fraction [%]	18.8	N/A	18.6	19.0	17.2	18.4	21.9
LS elevator defl. [deg]	-20.0	N/A	-20.0	-20.0	-20.0	-20.0	-20.0
LS inboard flap-elevon defl. [deg]	-12.3	N/A	-11.1	-12.5	-12.5	-11.7	-9.4
LS middle flap-elevon defl. [deg]	-2.5	N/A	-2.2	-2.0	-12.5	-3.5	-1.4
LS outboard flap-elevon defl. [deg]	-3.5	N/A	-3.9	-3.2	-12.5	-1.6	-1.1
Critical engine failure speed, V_{EF} [kt]	119.7	N/A	119.0	N/A	119.1	121.9	118.1
Takeoff rotation speed, V_R [kt]	125.1	N/A	124.6	N/A	125.4	130.5	121.6
Liftoff speed, AEO, $V_{LOF_{AEO}}$ [kt]	136.9	N/A	136.6	N/A	137.8	142.8	131.7
Liftoff speed, OEI, $V_{LOF_{OEI}}$ [kt]	129.8	N/A	129.3	N/A	130.3	135.6	125.8
Accel.-stop dist., AEO [ft]	5 410	N/A	5 410	N/A	5 410	5 410	5 240
Accel.-stop dist., OEI [ft]	4 860	N/A	4 840	N/A	4 800	4 730	4 890
Accel.-go dist. AEO [ft]	5 410	N/A	5 410	N/A	5 400	5 310	5 410
Accel.-go dist. OEI [ft]	5 410	N/A	5 410	N/A	5 410	5 410	5 410
Steady-climb speed, AEO, $V_{SC_{AEO}}$ [kt]	136.9	N/A	136.6	N/A	137.8	142.8	131.7
Steady-climb speed, OEI, $V_{SC_{OEI}}$ [kt]	129.8	N/A	129.4	N/A	130.3	135.7	125.9
Reference stall speed, V_S [kt]	115.1	N/A	114.7	N/A	115.6	111.3	111.6

* At aftmost CG but untrimmed.

Table 4 Inequality constraint values at the optimum, with constraint activity indicated by boldface text

Measurement Excludes →	Benchmark	Case 1 Off-design	Case 2 OEI-V_{MC_G}	Case 3 Takeoff	Case 4 LS K_n	Case 5 Var. gear	Case 6 Geo. free.
Top-of-climb rate of climb [ft/min]	979	300	964	300	1 058	1 341	674
Critical LS K_n [% MAC_0]	**-4.00**	N/A	**-4.00**	**-4.00**	N/A	**-4.00**	**-4.00**
TOFL [ft]	**5 410**	N/A	**5 410**	N/A	**5 410**	**5 410**	**5 410**
Min. (OEI) steady-climb angle [deg]	4.4	N/A	4.3	N/A	4.5	5.5	3.8
Liftoff-to-stall-speed ratio, AEO	1.19	N/A	1.19	N/A	1.19	1.28	1.18
Liftoff-to-stall-speed ratio, OEI	**1.13**	N/A	**1.13**	N/A	**1.13**	1.22	**1.13**
Steady-climb-to-stall-speed ratio, AEO	1.19	N/A	1.19	N/A	1.19	1.28	1.18
Steady-climb-to-stall-speed ratio, OEI	**1.13**	N/A	**1.13**	N/A	**1.13**	1.22	**1.13**
Rotation time, AEO [s]	2.67	N/A	2.71	N/A	2.74	2.53	**2.50**
Rotation time, OEI [s]	**2.50**	N/A	**2.50**	N/A	**2.50**	**2.50**	2.53
Ratio of V_R to V_1	1.01	N/A	1.01	N/A	1.02	1.03	**1.00**
Interior poly. vertical margins [ft]	**0.00**	**0.00**	**0.00**	**0.00**	**0.00**	**0.00**	**0.00**
Interior poly. aft perturb. margin [ft]	0.90	5.32	1.13	1.27	1.84	**0.00**	**0.00**
Wingtip-strike margin [ft]	1.33	**0.00**	1.35	1.17	**0.00**	**0.00**	0.82
Ground clearance margin [ft]	0.06	**0.00**	**0.00**	0.02	0.35	0.13	**0.00**
Wing dihedral [deg]	3.70	1.61	3.80	3.48	1.89	**4.00**	**4.00**
Winglet height [ft]	14.7	**7.1**	**5.0**	11.1	13.9	14.6	11.5
Excess wing volume [ft^3]	**0.00**	**0.00**	**0.00**	**0.00**	**0.00**	**0.00**	**0.00**
Centerbody excess width [ft]	0.30	0.28	0.30	0.25	0.26	0.89	2.04
Centerbody rounded nose	**Active**	**Active**	**Active**	**Active**	**Active**	Inactive	**Active**

The optimizer deflects each pitch control surface downward at the low-speed-flight analysis point in all but one case, which helps limit the angle of attack by contributing to the satisfaction of the lift constraint. The burden of zeroing the pitching moment is thus eased, as the aircraft optimized in this work have a positive dependence of pitching moment on angle of attack, at least at the low-speed-flight analysis point, as shown in Fig. 3. Another design difference that helps mitigate the angle of attack and therefore the pitching moment in the benchmark case is the planform area, which is 5.6% higher than that of case 1. In particular, increasing the planform area by lengthening the centerbody also increases the effectiveness of the elevator, and as discussed above, this control surface is particularly compatible with the static margin constraint.

The optimized position of the interior polyhedron leaves ample space for the optimizer to include centerbody leading-edge carving on the benchmark design and in several other cases. This design feature discussed by Sargeant et al. [64] helps efficiently trim a nose-heavy aircraft in pitch; it reduces the need to lower or reverse the lift load near the trailing edges, for example through reflexed airfoils. The effect of leading-edge carving can be seen in Fig. 4, where the cross-sections in question are more front-loaded due to a higher-pressure region near the leading edge. Leading-edge carving efficiently compensates for the measures taken to satisfy at least the low-speed static margin constraint, which requires a far-forward CG (and a far-aft neutral point).

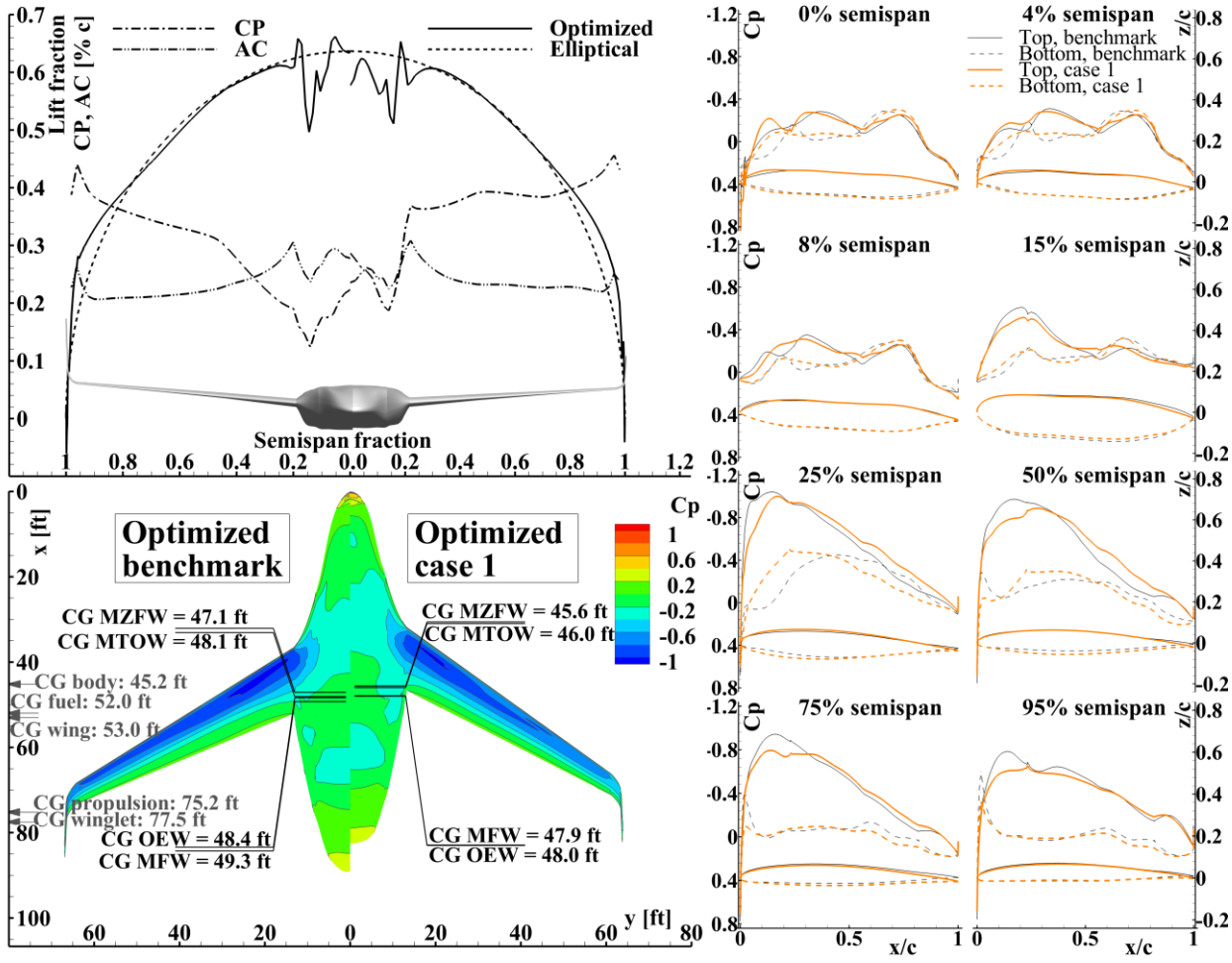

Fig. 4 Optimized benchmark and case 1 designs with cruise aerodynamic performance.

The wingtip chord length reaches the 5-ft lower bound in all cases, which happens at least in part because wing weight depends more strongly on wingtip chord length than winglet weight depends on height.

B. Design Features for Optimal Takeoff and Low-Speed Performance

In this section, cases 1 through 4 are analyzed to arrive at conclusions about specific elements of the benchmark design that are introduced to satisfy the takeoff and low-speed-flight design requirements.

1. Case 1: No Takeoff and Low-Speed-Flight Design Requirements

The characteristics of the optimized aircraft obtained in case 1 are included in Fig. 4. The block fuel burn penalty for simultaneously satisfying all takeoff and low-speed design requirements is 3.2%, and it is due to a 0.9% lower cruise lift-to-drag ratio and a 3.4% higher MTOW. The optimal wingspan is 3.5% longer in the benchmark case, the

wing sweep is 10.5% lower, and the wing root is located at 41.1% of the centerbody centerline instead of 38.6%. The optimizer is controlling these variables to trade between at least: neutral point, center-of-pressure, rudder, and CG positions, flap-elevon effectiveness, wing weight, and trim drag in the benchmark case, and between at least wing weight, CG position, and the active tip-strike margin in case 1.

Trim drag minimization is the primary driver for CG placement in this case, and only the cruise CG is thus implicitly constrained, so the total CG range is increased to 5.7% MAC_0. In the benchmark case, the centers of pressure are positioned particularly far forward compared to those in case 1, especially over the centerbody and blending segment; the aft portion of the airfoils contributes little to the total sectional lift. Such forward-biased centers of pressure help balance the optimized benchmark aircraft with its CG perturbed forward by 5.0% MAC_0, as opposed to 5.0% MAC_0 aft in case 1. As discussed in Section IV.A, at least some of the low-speed design requirements benefit from nose-heaviness, which renders optimal the forward-biased centers of pressure.

2. Case 2: No OEI-V_{MC_G} design requirement

The influence of the OEI-$V_{\mathrm{MC_G}}$ directional-trim constraint on optimal performance and most parameters of the optimal design is small, with the block fuel burn penalty for enforcing the constraint being 0.7% due to a 0.4% lower cruise lift-to-drag ratio and a 0.4% higher MTOW. In the benchmark case, the winglets are 2.9 times the height of those obtained in case 2, where height has hit a relaxed lower bound relative to that in case 1. Thus, winglet and rudder sizing strongly depend on an element of the problem definition that has a low impact on performance, which could be omitted in pure performance evaluation problems.

In all cases except case 1, the winglet is positioned farther forward than it would be if fins were installed on the aft centerbody instead. This observation suggests that a reduction in the total wetted area is possible through using fins, as was done by Reist et al. [7]. A net performance benefit may be obtainable through such a design change, and the optimizer may unsweep the less constrained wing and thus lighten it, but a net loss in performance is also possible through, for example knock-on implications such as the need to reinforce the nacelle structure in order to allow them to support a fin (little space is available to install the fins directly on top of the centerbody). In any case, the results of case 2 and those of Reist et al. [7] imply that the net effect on performance may again be small, so this aspect of the design is not further considered in this work.

3. Case 3: No Takeoff Design Requirements

The activity of the TOFL constraint, the OEI liftoff- and steady-climb-speed margins to stall speed, and the OEI rotation time constraint indicates the drivers of engine size. These constraints are all takeoff design requirements. Moreover, the dependence is strong: the engines produce 30.1% more SLS thrust in the benchmark case than in case 3. In case 3, the optimizer compensates for the lighter engines located well aft of all CGs by rebalancing the contributions to the CGs and neutral point such that the design is overall more fuel-efficient; the block fuel burn is 0.5% higher and MTOW is 2.2% higher in the benchmark case. Although the cruise lift-to-drag ratio is 1.0% higher in the benchmark case, lighter engines remain favorable because the optimizer is effectively maximizing a ratio of L/D to weight in its minimization of block fuel burn.

4. Case 4: No Low-Speed Static Margin Design Requirement

The pitch control surfaces again act as plain flaps in case 4 and limit the angle of attack required to achieve trim while producing a net nose-down pitching moment. Both effects ease the pitch trim problem for this longitudinally unstable aircraft. In contrast to the benchmark case, each pitch control surface is saturated downward at the low-speed-flight analysis point in case 4, and, as shown in Fig. 5, many aerodynamic centers are located far forward as a result. The net effect is an (unconstrained) low-speed static margin of -20.6% MAC_0 (nonetheless, the cruise static margin perturbed to consider the aftmost CG is -1.33% MAC_0). These observations suggest that the flap-elevons are too destabilizing when deflected beyond the angles used in the benchmark case, where trim is achieved through other means, namely increased elevator effectiveness through centerbody lengthening.

The OEW CG is perturbed forward by 1.12% MAC_0 in case 4, as opposed to 5.0% MAC_0 in the benchmark case, which indicates that the static margin constraint is indeed a driver of a nose-heavy design. Since the bound is reached in the benchmark case, at least some proportion of the static margin constraint is satisfied through nose-heaviness and the remainder is satisfied through aft neutral point movement. The OEW CG is perturbed aft by 5.0% MAC_0 in case 1. This perturbation more than compensates for the forward CG movement due to the smaller engines, which suggests that the (absent) low-speed pitching moment constraint is another driver of a forward-positioned CG. Indeed, fewer design perturbations are thus needed to increase the effectiveness of the saturated pitch control surfaces in case 4.

Several compensatory design features arise in response to the need to trim the nose-heaviness. Leading-edge carving appears on several optimal geometries, corroborating the conclusion of Sargeant et al. [64] stating that this

design feature is relatively efficient. This design feature is not observed in case 1, where few and insignificant compensatory design perturbations are required to trim the pitching moment when the OEW CG perturbation design variable is fully and solely used to help minimize trim drag. A small ridge is formed near the front of the centerbody, but this design feature is absent on the geometry from case 4, so it can be attributed to the relatively efficient satisfaction of the static margin constraint. A comparison of the pressure-coefficient plots and contours shown in Fig. 5, which pertain to the low-speed-flight analysis point for the benchmark case and for case 4, suggests that the ridge locally increases lift. In the benchmark case, the low-pressure regions extend father toward the nose than in case 4. Thus, the centerbody is more front-loaded, suggesting that the ridge at least behaves similarly to centerbody leading-edge carving: it helps move the centers of pressure forward, thus allowing for additional stabilizing forward CG movement while at least reducing the need to generate downward loads behind the CG. Since little to no lift reduction is required to trim the aircraft, a reduction in the planform area is thus achieved. If net additional lift were generated, it would further help reduce the planform area and aircraft weight; however, the absence of the ridge in case 4, which includes the low-speed lift constraint, suggests that generating significant net additional lift is at least not the main purpose of the ridge. No geometric constraint artificially drives the formation of the ridge; for example, the leading-edge carving does not cause the ridge to appear on the upper surface due to a local section thickness constraint. Vortices are generated at the ridge at the high angle of attack used at the low-speed-flight analysis point, and they traverse the centerbody and connect to the vortices generated on its trailing edge. Further investigation is needed to determine whether these vortices produce net vortex lift or help delay flow separation over the downward-saturated elevator at low speeds.

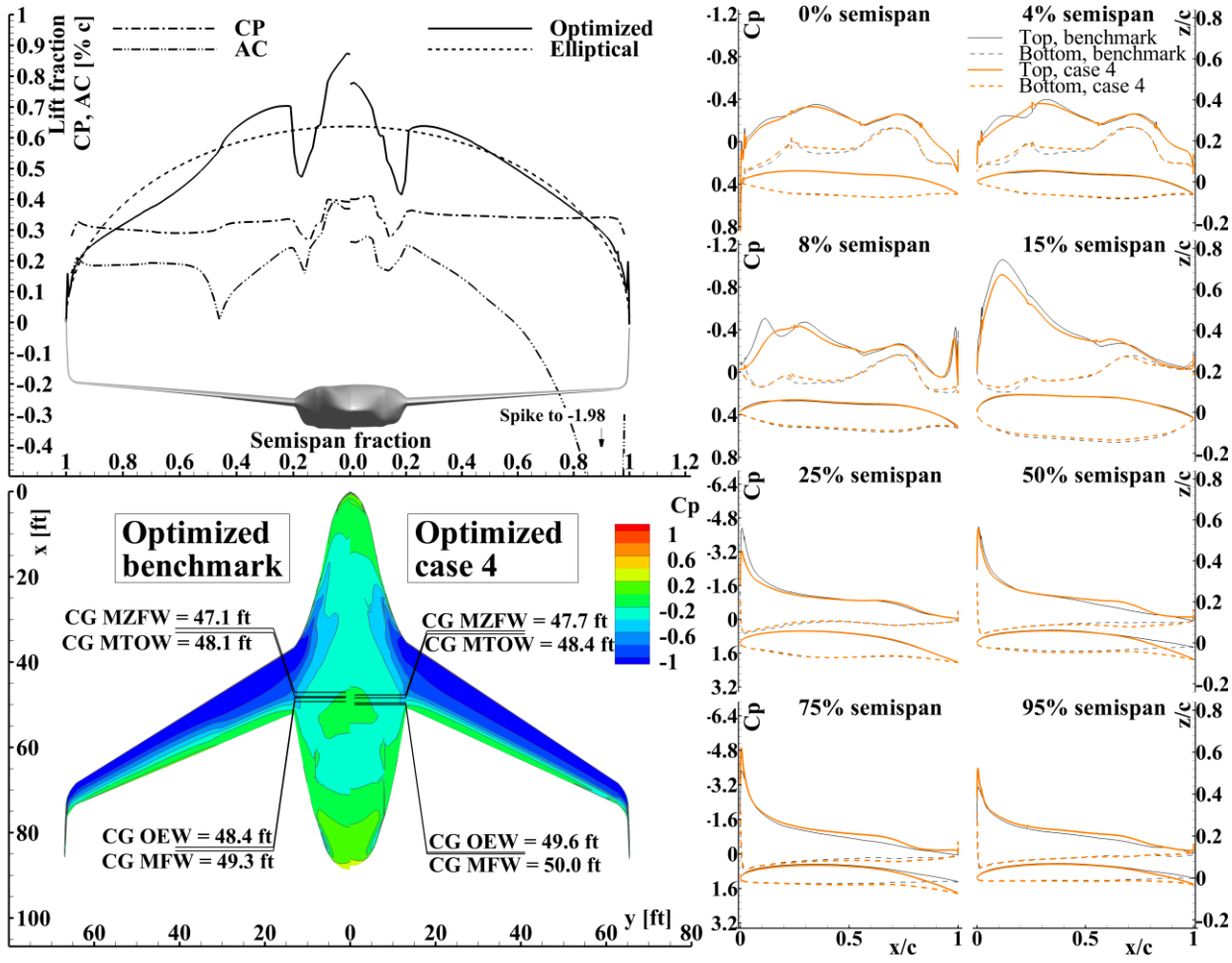

Fig. 5 Optimized benchmark and case 4 designs with low-speed aerodynamic performance.

C. Design Features for Optimal Performance with Conventional Landing Gear

In case 5, the need to produce a supplementary pitching moment at the additional takeoff rotation analysis point beyond what can be produced by the pitch control surfaces alone drives the optimal design far from that obtained in the benchmark case. Consequently, the block fuel burn is 5.0% higher than in the benchmark case despite the 0.4% increase in the cruise lift-to-drag ratio because of the 6.0% higher MTOW. Requiring a regional-class BWB aircraft to rotate about conventionally positioned main landing gear remains punitive, despite the following targeted modifications to the problem definition when compared to that of Ref. [7]: 1) higher OML geometric freedom, 2) higher limits on the pitch control surface deflections, i.e. 80% instead of 33% for the elevator and 50% instead of

33% for the flap-elevons, 3) engines positioned at 0.5 instead of 1.5 nacelle diameters above the aft centerbody, and 4) an optimizable takeoff rotation speed.

Many aspects of the problem definition are leveraged to help satisfy the rotation constraint; many of the design features and perturbations from the benchmark design, which are discussed below, increase the moment arm between the centers of pressure and the main landing gear. First, 1) leading-edge carving extends from the wing root into the blending segment, where it is more pronounced than in the benchmark case, as shown on the 15%-semispan pressure coefficient plot in Fig. 6, and 2) the distance between the wing root leading edge and the main landing gear (if conventional landing gear had been used in the benchmark case) is increased from 34.8% to 45.6% MAC_0 while other aspects of the wing root geometry remain similar. Thus, the aircraft is particularly aerodynamically front-loaded in case 5.

Second, the wingspan is 12.5% longer, which enlarges the flap-elevons, and the wing sweep is 12.0% higher, which combines with the higher wingspan and forward wing root position to locate the center of pressure of the wing segment housing the inboard flap-elevon farther forward and that housing the outboard flap-elevon farther aft, thus increasing the effectiveness of these pitch control surfaces. The increased wing sweep combined with the higher wingspan also helps compensate for destabilizing aspects of the design such as the far forward wing root position. The centerbody width negligibly increases despite the high effectiveness of the elevator at least in part because its weight grows rapidly with respect to width compared to the growth rate of wing weight with respect to wingspan. Compared to case 6, where both the centerbody width and the wingspan have increased, the high geometric freedom available in case 5 helps avoid even more punitive methods of supplementing the pitching moment, which would have been required if case 6 had considered a takeoff rotation constraint. Moreover, the optimizer leverages a venturi effect in the convergence zone between the lower aft-centerbody and the ground to locally lower the pressure behind the main landing gear and thus increase the pitching moment; this could become problematic at the instant of liftoff due to the additional lift required to compensate for the downward load. In summary, the optimizer controls the locations of the centers of pressure relative to the main landing gear.

Third, the SLS thrust is increased by 18.4% relative to the benchmark case at least in part because a 4.3% higher V_R can thus be achieved despite the higher MTOW, thus making the pitch control surfaces more effective. Moreover, the thrust-line angle reaches its bound of -2° to reduce the moment of thrust about the main landing gear.

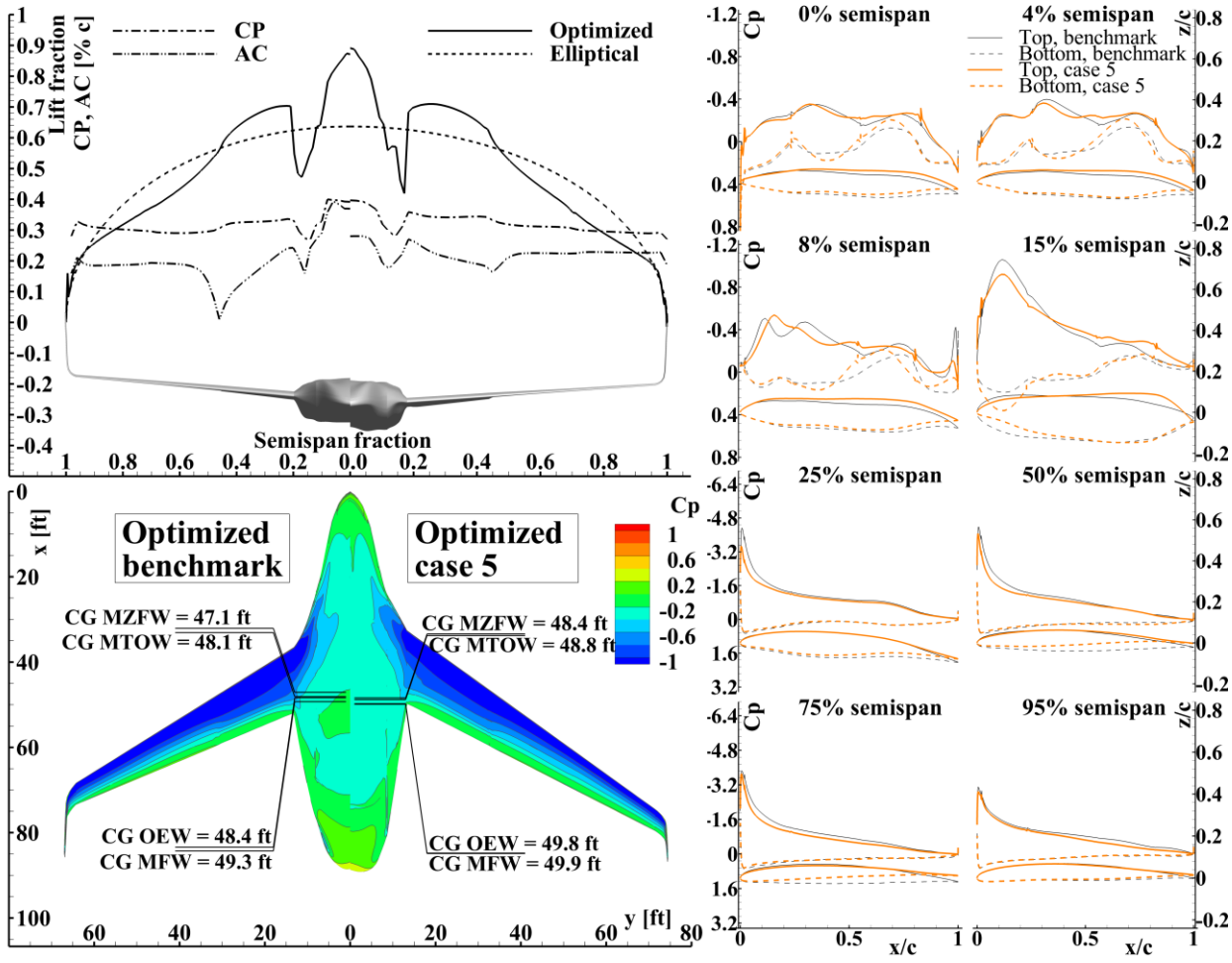

Fig. 6 Optimized benchmark and case 5 designs with low-speed aerodynamic performance.

The aforementioned methods of satisfying the rotation constraint are numerous. They are overall more efficient than the methods reported by Reist et al. [7], where a block fuel burn penalty of 9.6% is measured. In that work, fewer design requirements are imposed; it considers 1) a cruise static margin constraint, 2) the OEI-$V_{\mathrm{MC_G}}$ directional trim constraint, and 3) the takeoff rotation constraint, yet the optimizer resorts to punitive means of reaching a feasible design, at least because 1) a lower (33%) saturation limit is used for the pitch control surfaces, 2) variable-length landing gear is not considered, 3) the engines are mounted 1.5 nacelle diameters above the aft centerbody, and 4) the geometric freedom is restricted and similar to that of case 6. These four limitations of the problem definition, which are addressed in this work, enable the optimizer to satisfy several additional design requirements without severely compromising block fuel burn.

D. Design Features for Optimal Performance with Lower Geometric Freedom

In general, the optimizer uses the high geometric freedom to tailor each controlled cross-section to efficiently satisfy the design requirements. For example, the high centerbody cross-section freedom is used to tightly wrap the outer mold line around the interior polyhedron in all cases except case 6, where the forebody ridge is not observed and the centerbody leading-edge carving is less pronounced. The higher geometric freedom improves block fuel burn by 4.1% in the benchmark case due to a 3.0% higher cruise lift-to-drag ratio and a 1.8% lower MTOW. This result suggests that performing typical conceptual design using preselected airfoils and lower-fidelity aerodynamics calculations such as panel or vortex-lattice codes that exclude flow nonlinearities would exclude significant mechanisms that could be leveraged to satisfy the design requirements more efficiently. Moreover, a 5.3% decrease in wetted area, a 7.7% decrease in planform area, and a 4.0% decrease in wingspan are observed in the benchmark case.

V. Sensitivity Studies

Two design-sensitivity studies are discussed in this section. First, since the negative static margin of -4% MAC_0 would require active stabilization, it is useful to consider the trade-off between the static margin bound and the optimal performance; cases A1 and A2 are solved with a bound of 0% MAC_0 and 4% MAC_0, respectively. Second, since the elevator has reached its 80% deflection limit at the trim-critical low-speed-flight analysis point in the benchmark case, thus leaving only 20% of its maximum downward deflection for low-speed pitch control, it is useful to examine the trade between controllability and the satisfaction of the low-speed trim and static margin constraints. For that reason, the elevator deflection limit is lowered to 65% in case B1 and 50% in case B2, respectively, while the flap-elevon defection limit is maintained at 50%. Key results from both sensitivity studies are shown in Table 5.

A. Design Sensitivity to the Low-Speed Static Margin Requirement

Table 5 shows that the optimal performance depends modestly on the static margin bound, and Fig. 7 shows that some elements of the optimal design depend strongly on this design requirement. In particular, the shorter wingspan of 124.0 ft obtained in case A2 is closer to the code-C gate limit of 118.0 ft, and the 1.7% increase in block fuel burn can be considered small. The wing root is moved aft likely to move the neutral point aft. Moreover, the aerodynamic centers on the centerbody are moved aft, thus helping stabilize the aircraft.

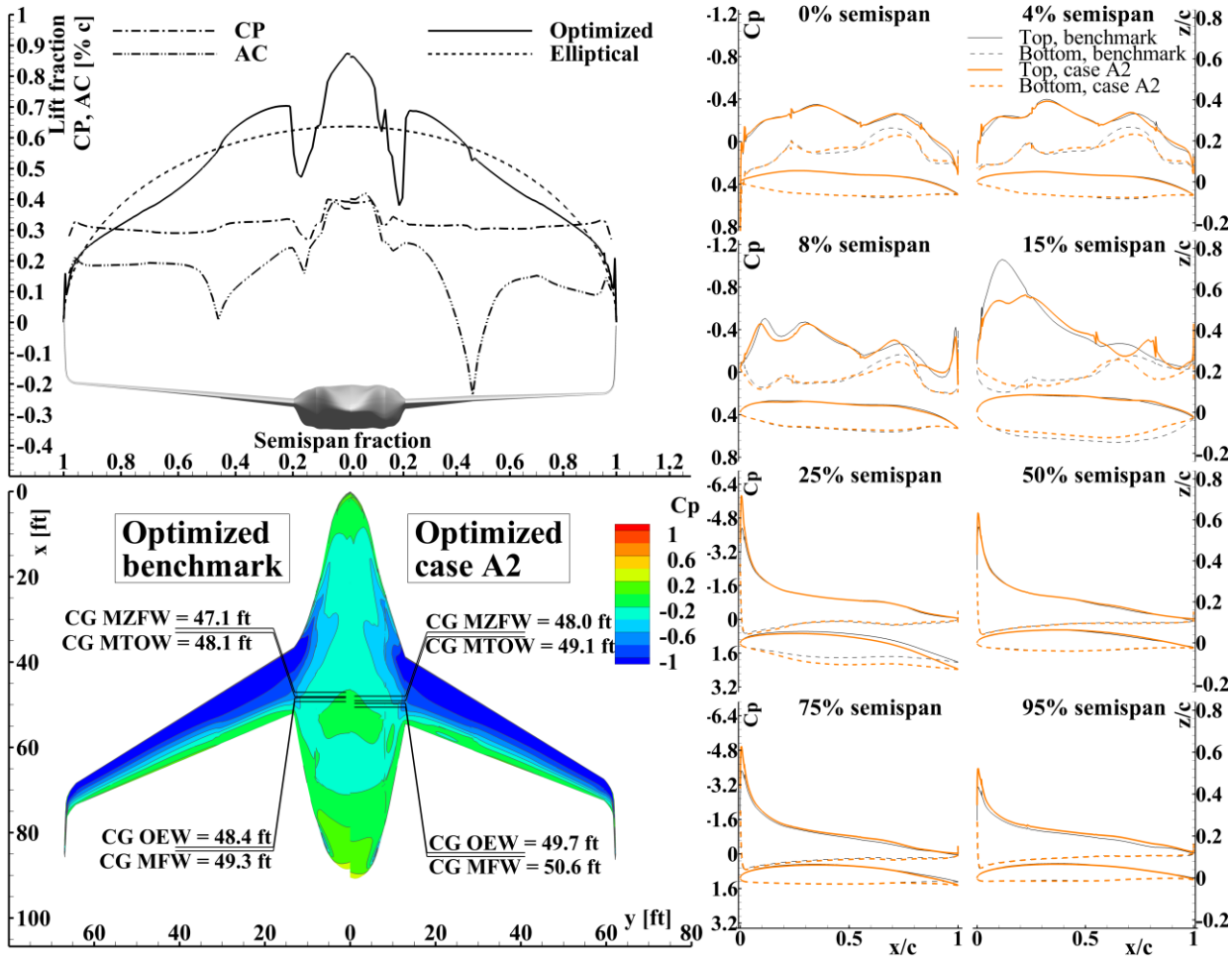

Fig. 7 Optimized benchmark and case A2 designs with low-speed aerodynamic performance.

The optimized design obtained in case A2 is driven far from the benchmark optimized design, unlike in case A1. Conversely, the cost in terms of block fuel burn to reach the neutrally stable design is higher than the cost to go from the neutrally stable design to the design with the positive static margin. To investigate whether multimodality explains this trend, case A2 was started from three different initial designs, one starting point being the optimized design from case A1, but every test yielded the same result.

Table 5 Design-sensitivity study results relative to the benchmark case

	Case A1 $K_n \geq 0\%$ MAC_0	Case A2 $K_n \geq 4\%$ MAC_0	Case B1 65% elev.	Case B2 50% elev.
Block fuel burn [%]	+1.1	+1.7	+0.2	+0.3
Cruise L/D [%]	−1.1	−2.4	−0.1	−0.4
MTOW [%]	+0.2	−0.1	+0.1	−0.1
Wingspan [%]	+0.4	−5.9	+2.1	+1.9
Centerbody length [%]	+1.2	+2.3	−0.1	−0.5

B. Low-Speed Trim, Stability, and Control Trade-Offs

Results show that the optimal performance is nearly independent of the elevator deflection limit, at least between 80% and 50%, and that favorable design characteristics are unsurprisingly positively correlated with the elevator deflection limit. However, the effect is smaller than that observed in a similar sensitivity study conducted with a conventional takeoff rotation constraint and similar design freedom in Ref. [8]. Since a 50%-50% control allocation, as opposed to the benchmark 80%-50% leads to a design with very similar performance, confidence is high that appropriate deflection limits that provide an adequate control margin can be found at little cost to performance even if the considered allocations prove excessive. As the elevator effectiveness is reduced, the flap-elevons are not deflected significantly more; as shown in Fig. 5, this would be destabilizing. Indeed, case B2 increases the downward deflection of the inboard, middle, and outboard flap-elevons by only 0.2°, 1.2°, and 0.7°, respectively. Instead, the centerbody is shortened by 0.5%, which reduces its weight and its contribution to friction drag, which are less favorably traded when the attached elevator is less effective, and the wingspan is lengthened by 1.9%, which increases the effectiveness of the flap-elevons at any given deflection angle. Moreover, the engine is 0.7% lighter, which helps reduce the burden of trimming the pitching moment with a less effective elevator.

VI. Conclusions

The high potential fuel-efficiency of the BWB unconventional aircraft configuration makes it a well-ranked candidate in the global effort to reduce the impact of civil aviation on climate change. Although low- to medium-fidelity conceptual-level tools can provide an accurate energy-efficiency estimate for the CTW configuration, they are more limited for tightly integrated unconventional configurations. This work shows that several complex multidisciplinary design challenges unique to the BWB configuration can be effectively addressed through a mixed-fidelity MDO framework that includes a high-fidelity aerodynamics model coupled with high design freedom. This framework is particularly adept at simultaneously satisfying several design requirements.

This work expands upon previous work through 1) the imposition of additional critical design requirements, namely the constraints on takeoff and initial-climb performance, and on the critical low-speed trim and static margin, 2) the quantification of the impact of the critical design requirements on the optimal design and its performance, and 3) the use of higher design freedom, namely the nonlinear spanwise variation of cross-section design variables, the interior polyhedron position and orientation, the OEW CG freedom, the thrust-line angle, and the increased pitch control surface deflection limits, and 4) the measurement of the design sensitivity to the low-speed static margin bound and the low-speed controllability margin.

The optimized regional-class BWB aircraft obtained in this work, i.e., the benchmark design, has a specific fuel burn of 0.0619 lb/pax/nmi, a cruise lift-to-drag ratio of 21.7, and an MTOW of 111 900 lb, which is lighter than the 124 300-lb Embraer E190-E2. This level of performance is attained at least in part through design features that are novel and particularly effective for the BWB configuration, which are included in the highly multidimensional design space. These include the centerbody leading-edge carving and forebody ridge that help efficiently trim the aircraft with CGs positioned farther forward than would otherwise be optimal, thus helping to satisfy the low-speed pitch-trim and static margin constraints. Moreover, the underdetermined low-speed trim problem provides analysis-point-specific design variables that are leveraged to maximize the static margin and thus lessen the impact of this constraint on performance at other stages of flight. The importance of high geometric freedom in BWB aircraft design is highlighted in case 6, where the cross-section geometric freedom of the centerbody and blending segment is made reminiscent of the conceptual phase of aircraft design at a 4.3% cost to block fuel burn.

The effect of several performance-based design requirements is investigated in this work. Ranked from the most to the least significant in terms of their effect on the design-mission block fuel burn, the constraints considered are the following: 1) the takeoff rotation constraint when variable-length landing gear is excluded, with a penalty of 5.0%, 2) the low-speed static margin constraint, with a penalty of 1.5%, 3) the OEI-$V_{\mathrm{MC_G}}$ directional-trim constraint, with a penalty of 0.7%, and 4) the takeoff and initial-climb constraints, with a combined penalty of 0.5%.

The block fuel burn penalty associated with the conventional rotation mechanism remains significant despite the mitigating measures taken; namely 1) higher OML geometric freedom, 2) higher limits on the pitch control surface deflections, i.e. 80% instead of 33% for the elevator and 50% instead of 33% for the flap-elevons, 3) engines positioned at 0.5 instead of 1.5 nacelle diameters above the centerbody, and 4) an optimizable takeoff rotation speed, so variable-length landing gear appears to be significant to the success of regional-class BWB aircraft. Future work

could investigate knock-on effects enabled by this mechanism; namely, the wing weight model could be recalibrated to exclude slats, which may not be needed, as field performance is improved through lower liftoff speeds (at any given angle of attack) when significant downward loads must not be generated in order to produce the pitching moment needed to achieve takeoff rotation.

Two sensitivity studies lead to the conclusions that 1) the benchmark design is modestly sensitive to the imposed static margin bound, with the block fuel burn penalty associated with attaining a 4%-MAC_0 positive static margin being 1.7%, and 2) the benchmark design (in which variable-length landing gear is used) is almost insensitive to the elevator deflection limit, with the block fuel burn penalty being only 0.3% when defining saturation as a 50% deflection instead of 80%.

A further increase in credibility could be obtained in future work by testing some of the assumptions made in this work, namely the absence of buffet and flutter considerations and the lack of variability in cruise operating conditions. Higher-fidelity models would also serve the same purpose while also increasing design freedom potential and allowing for less conservatism. For example, they could circumvent the limitations implicit in the geometrically fixed interior polyhedron whose weight model gives only two variables to exploit (MTOW and the pressurized projected area). Moreover, modeling engine-OML aerodynamic interactions would more exactly guide the decision on engine positioning and spacing. The relationship between the cabin layout and the optimal cruise altitude could also be investigated. In addition, geometric freedom could be further increased: two targeted areas for improvement are the inclusion of a wing crank within the design space and flap-elevons with unequal span fractions, both of which could (at least) ease the burden of satisfying the low-speed trim and static margin constraints. Moreover, the problem formulation developed in this work could be applied to the single-aisle and twin-aisle aircraft classes to determine whether the conclusions generalize to larger aircraft, and BWB aircraft could be compared with equivalent CTW aircraft.

Appendix: Compensation for Aerodynamic Functional Errors on Coarse Grids

If the ratio of an aerodynamic coefficient calculated via Richardson extrapolation to the aerodynamic coefficient calculated on a finite-size grid is nearly independent of small geometric changes, which is found to be the case if the initial and optimized geometries are similar, it can be used as a correction factor during optimization to account for discretization errors. This correction is especially useful for accurate fuel-burn calculations, as drag is significantly

and increasingly overpredicted as the grid is coarsened. The performance values reported in Table 3 correspond to the corrected aerodynamic coefficients. The correction factors computed between the penultimate and final optimization stages are given in Table 6.

Table 6 Final aerodynamic force and moment (about the nose) correction factors used during optimization

		D				Y	L			$m^{(0)}$			$n^{(0)}$
		Free air		Ground		Ground	Free air		Ground	Free air		Ground	Ground
Grid	Node count†	Cruise	LS	OEI	Rot.	OEI	Cruise	LS	Rot.	Cruise	LS	Rot.	OEI
L0	325 248	0.656	0.831	0.602	0.745	1.047	1.029	1.104	0.896	1.030	1.109	0.896	0.955
L1	562 432	0.716	0.860	0.642	0.775	0.996	1.019	1.077	0.928	1.020	1.079	0.928	0.999
L2	1 048 576	0.782	0.884	0.700	0.813	0.935	1.012	1.051	0.955	1.013	1.051	0.955	1.119
L3	2 314 368	0.859	0.910	0.782	0.864	0.924	1.007	1.027	0.975	1.007	1.026	0.975	1.155
L4	4 412 928	0.911	0.937	0.848	0.901	0.937	1.004	1.017	0.984	1.005	1.016	0.984	1.128
L5	8 388 608	0.946	0.959	0.901	0.929*	0.953	1.002	1.011	0.990*	1.003	1.010	0.990*	1.093
L6	17 428 608	0.968*	0.973*	0.938	N/A	0.967	1.001*	1.007*	N/A	1.002*	1.006*	N/A	1.063
L7	34 707 744	N/A	N/A	0.960*	N/A	0.979*	N/A	N/A	N/A	N/A	N/A	N/A	1.039*
Richardson		1.000	1.000	1.000	1.000	1.000	1.000	1.000	1.000	1.000	1.000	1.000	1.000

* Finest grid used for Richardson extrapolation.
† Node count is slightly higher for on-ground analyses.

Acknowledgments

This research was enabled in part by the support provided by Compute Ontario (computeontario.ca) and the Digital Research Alliance of Canada (alliancecan.ca); computations were performed on the Niagara supercomputer. Financial support was provided by the Natural Sciences and Engineering Research Council of Canada, Bombardier Aerospace, Transport Canada, and the University of Toronto.

References

[1] Bravo-Mosquera, P.D., Catalano, F.M., and Zingg, D.W., "Unconventional Aircraft for Civil Aviation: A Review of Concepts and Design Methodologies," *Progress in Aerospace Sciences*, Vol. 131, 2022. https://doi.org/10.1016/j.paerosci.2022.100813

[2] Anon., "Aircraft Technology Net Zero Roadmap," International Air Transport Association, 2023, https://www.iata.org/contentassets/8d19e716636a47c184e7221c77563c93/aircraft-technology-net-zero-roadmap.pdf [retrieved 29 Jul. 2023].

[3] Callaghan, J.T., and Liebeck, R.H., "Some Thoughts on the Design of Subsonic Transport Aircraft for the 21st Century," *SAE Transactions: Journal of Aerospace*, Vol. 99, No. 2, 1990, pp. 2104–2111. https://doi.org/10.4271/901987

[4] Liebeck, R.H., "Design of the Blended Wing Body Subsonic Transport," *Journal of Aircraft*, Vol. 41, No. 1, 2004, pp. 10–25. https://doi.org/10.2514/1.9084

[5] Chau, T., and Zingg, D.W., "Aerodynamic Shape Optimization of a Box-Wing Regional Aircraft Based on the Reynolds-Averaged Navier-Stokes Equations," *35th AIAA Applied Aerodynamics Conference*, AIAA Paper 2017-3258. https://doi.org/10.2514/6.2017-3258

[6] Reist, T.A., and Zingg, D.W., "High-Fidelity Aerodynamic Shape Optimization of a Lifting-Fuselage Concept for Regional Aircraft," *Journal of Aircraft*, Vol. 54, No. 3, 2017, pp. 1085–1097. https://doi.org/10.2514/1.C033798

[7] Reist, T.A., Zingg, D.W., Rakowitz, M., Potter, G., and Banerjee, S., "Multifidelity Optimization of Hybrid Wing–Body Aircraft with Stability and Control Requirements," *Journal of Aircraft*, Vol. 56, No. 2, 2019, pp. 442–456. https://doi.org/10.2514/1.C034703

[8] Gray, A.L., Reist, T.A., and Zingg, D.W., "Further Exploration of Regional-Class Hybrid Wing-Body Aircraft Through Multifidelity Optimization," *AIAA SciTech 2021 Forum*, AIAA Paper 2021-0014, Jan. 2021. https://doi.org/10.2514/6.2021-0014

[9] Zingg, D.W., Chau, T., Gray, A.L., and Reist, T.A., "A Multifidelity Multidisciplinary Approach to Unconventional Aircraft Development and Assessment with Application to the Strut-Braced-Wing and Hybrid-Wing-Body Configurations," *33rd Congress of the International Council of the Aeronautical Sciences*, ICAS Paper 0748, Sept. 2022.

[10] Bravo-Mosquera, P.D., Chau, T., Catalano, F.M., and Zingg, D.W., "Exploration of Box-Wing Aircraft Concept Using High-Fidelity Aerodynamic Shape Optimization," *33rd Congress of the International Council of the Aeronautical Sciences*, ICAS Paper 0446, Sept. 2022.

[11] Chau, T., and Zingg, D.W., "Aerodynamic Design Optimization of a Transonic Strut-Braced-Wing Regional Aircraft," *Journal of Aircraft*, Vol. 59, No. 1, 2022, pp. 253–271. https://doi.org/10.2514/1.C036389

[12] Chau, T., and Zingg, D.W., "Fuel Burn Evaluation of a Transonic Strut-Braced-Wing Regional Aircraft through Multipoint Aerodynamic Optimisation," *The Aeronautical Journal*, Vol. 127, No. 1308, 2023, pp. 305–329. https://doi.org/10.1017/aer.2022.64

[13] Chau, T., and Zingg, D.W., "Aerodynamic Optimization and Fuel Burn Evaluation of a Transonic Strut-Braced-Wing Single-Aisle Aircraft," *Journal of Aircraft*, Vol. 60, No. 5, 2023, pp. 1638–1658. https://doi.org/10.2514/1.C037158

[14] Qin, N., Vavalle, A., and Le Moigne, A., "Spanwise Lift Distribution for Blended Wing Body Aircraft.," *Journal of Aircraft*, Vol. 42, No. 2, 2005, pp. 356–365. https://doi.org/10.2514/1.4229

[15] Peigin, S., and Epstein, B., "Computational Fluid Dynamics Driven Optimization of Blended Wing Body Aircraft," *AIAA Journal*, Vol. 44, No. 11, 2006, pp. 2736–2745. https://doi.org/10.2514/1.19757

[16] Kuntawala, N., Hicken, J., and Zingg, D., "Preliminary Aerodynamic Shape Optimization of a Blended-Wing-Body Aircraft Configuration," *49th AIAA Aerospace Sciences Meeting including the New Horizons Forum and Aerospace Exposition*, AIAA Paper 2011-642, Jan. 2011. https://doi.org/10.2514/6.2011-642

[17] Méheut, M., Arntz, A., and Carrier, G., "Aerodynamic Shape Optimizations of a Blended Wing Body Configuration for Several Wing Planforms," *30th AIAA Applied Aerodynamics Conference*, AIAA Paper 2012-3122, June 2012. https://doi.org/10.2514/6.2012-3122

[18] Yang, S., Page, M., and Smetak, E.J., "Achievement of NASA New Aviation Horizons N+2 Goals with a Blended-Wing-Body X-Plane Designed for the Regional Jet and Single-Aisle Jet Markets," *2018 AIAA Aerospace Sciences Meeting*, AIAA Paper 2018-0521, Jan. 2018. https://doi.org/10.2514/6.2018-0521

[19] Greitzer, E.M., Bonnefoy, P.A., Hall, D.K., Hansman, R.J., Hileman, J.I., Liebeck, R.H., Lovegren, J., Mody, P., Pertuze, J.A., Sato, S., Spakovszky, Z.S., Tan, C.S., Hollman, J.S., Duda, J.E., Fitzgerald, N., Houghton, J., Kerrebrock, J.L., Kiwada, G.F., Kordonowy, D., Parrish, J.C., Tylko, J., and Wen, E.A., "N+3 Aircraft Concept Designs and Trade Studies, Final Report," NASA CR-2010-216794/VOL1, Dec. 2010.

[20] Lyu, Z., and Martins, J.R.R.A., "Aerodynamic Design Optimization Studies of a Blended-Wing-Body Aircraft," *Journal of Aircraft*, Vol. 51, No. 5, 2014, pp. 1604–1617. https://doi.org/10.2514/1.C032491

[21] Vicroy, D., "Blended-Wing-Body Low-Speed Flight Dynamics: Summary of Ground Tests and Sample Results (Invited)," *47th AIAA Aerospace Sciences Meeting and Exhibit*, AIAA Paper 2009-0933, Jan. 2009. https://doi.org/10.2514/6.2009-933

[22] Cook, M.V., and de Castro, H.V., "The Longitudinal Flying Qualities of a Blended-Wing-Body Civil Transport Aircraft," *The Aeronautical Journal*, Vol. 108, No. 1080, 2004, pp. 75–84. https://doi.org/10.1017/S0001924000005029

[23] Garmendia, D.C., Chakraborty, I., and Mavris, D.N., "Method for Evaluating Electrically Actuated Hybrid Wing–Body Control Surface Layouts," *Journal of Aircraft*, Vol. 52, No. 6, 2015, pp. 1780–1790. https://doi.org/10.2514/1.C033061

[24] Wakayama, S., "Multidisciplinary Design Optimization of the Blended-Wing-Body," *7th AIAA/USAF/NASA/ISSMO Symposium on Multidisciplinary Analysis and Optimization*, AIAA Paper 1998-4938, Sept. 1998. https://doi.org/10.2514/6.1998-4938

[25] Wakayama, S., "Blended-Wing-Body Optimization Problem Setup," *8th Symposium on Multidisciplinary Analysis and Optimization*, AIAA Paper 2000-4740, Sept. 2000. https://doi.org/10.2514/6.2000-4740

[26] Morris, A., "MOB A European Distributed Multi-Disciplinary Design and Optimisation Project," *9th AIAA/ISSMO Symposium on Multidisciplinary Analysis and Optimization*, AIAA Paper 2002-5444, Sept. 2002. https://doi.org/10.2514/6.2002-5444

[27] Hileman, J.I., Spakovszky, Z.S., Drela, M., Sargeant, M.A., and Jones, A., "Airframe Design for Silent Fuel-Efficient Aircraft," *Journal of Aircraft*, Vol. 47, No. 3, 2010, pp. 956–969. https://doi.org/10.2514/1.46545

[28] Brown, M., and Vos, R., "Conceptual Design and Evaluation of Blended-Wing Body Aircraft," *2018 AIAA Aerospace Sciences Meeting*, AIAA Paper 2018-0522, Jan. 2018. https://doi.org/10.2514/6.2018-0522

[29] Reist, T.A., "Scaling of Hybrid Wing-Body-Type Aircraft: Exploration Through High-Fidelity Aerodynamic Shape Optimization," Ph.D thesis, University of Toronto Institute for Aerospace Studies, Toronto, ON, Canada, 2016.

[30] Page, M.A., "Tilting Landing Gear Systems and Methods," Patent US 2018/0001999 A1, 1 April 2018.

[31] Hicken, J.E., and Zingg, D.W., "Aerodynamic Optimization Algorithm with Integrated Geometry Parameterization and Mesh Movement," *AIAA Journal*, Vol. 48, No. 2, 2010, pp. 400–413. https://doi.org/10.2514/1.44033

[32] Gagnon, H., and Zingg, D.W., "Two-Level Free-Form and Axial Deformation for Exploratory Aerodynamic Shape Optimization," *AIAA Journal*, Vol. 53, No. 7, 2015, pp. 2015–2026. https://doi.org/10.2514/1.J053575

[33] Osusky, M., and Zingg, D.W., "Parallel Newton–Krylov–Schur Flow Solver for the Navier–Stokes Equations," *AIAA Journal*, Vol. 51, No. 12, 2013, pp. 2833–2851. https://doi.org/10.2514/1.J052487

[34] Gill, P.E., Murray, W., and Saunders, M.A., "SNOPT: An SQP Algorithm for Large-Scale Constrained Optimization," *SIAM Journal of Optimization*, Vol. 12, No. 4, 2002, pp. 979–1006. https://doi.org/10.1137/S0036144504446096

[35] Jameson, A., "Aerodynamic Design via Control Theory," *Journal of Scientific Computing*, Vol. 3, No. 3, 1988, pp. 233–260. https://doi.org/10.1007/BF01061285

[36] Osusky, L., Buckley, H., Reist, T., and Zingg, D.W., "Drag Minimization Based on the Navier–Stokes Equations Using a Newton–Krylov Approach," *AIAA Journal*, Vol. 53, No. 6, 2015, pp. 1555–1577. https://doi.org/10.2514/1.J053457

[37] Reist, T.A., Koo, D., Zingg, D.W., Bochud, P., Castonguay, P., and Leblond, D., "Cross Validation of Aerodynamic Shape Optimization Methodologies for Aircraft Wing-Body Optimization," *AIAA Journal*, Vol. 58, No. 6, 2020, pp. 2581–2595. https://doi.org/10.2514/1.J059091

[38] Truong, A.H., Oldfield, C.A., and Zingg, D.W., "Mesh Movement for a Discrete-Adjoint Newton-Krylov Algorithm for Aerodynamic Optimization," *AIAA Journal*, Vol. 46, No. 7, 2008, pp. 1695–1704. https://doi.org/10.2514/1.33836

[39] Allmaras, S.R., Johnson, F.T., and Spalart, P.R., "Modifcations and Clarifcations for the Implementation of the Spalart-Allmaras Turbulence Model," *Seventh International Conference on Computational Fluid Dynamics*, Paper ICCFD7-1902, July 2012.

[40] Spalart, P., and Allmaras, S., "A One-Equation Turbulence Model for Aerodynamic Flows," *30th Aerospace Sciences Meeting and Exhibit*, AIAA Paper 1992-439, Jan. 1992. https://doi.org/10.2514/6.1992-439

[41] Spalart, P.R., "Strategies for Turbulence Modelling and Simulations," *International Journal of Heat and Fluid Flow*, Vol. 21, 2000, pp. 252–263. https://doi.org/10.1016/S0142-727X(00)00007-2

[42] Osusky, M., Boom, P.D., and Zingg, D.W., "Results from the Fifth AIAA Drag Prediction Workshop Obtained with a Parallel Newton-Krylov-Schur Flow Solver Discretized Using Summation-by-Parts Operators," *31st AIAA Applied Aerodynamics Conference*, AIAA Paper 2013-2511, June 2013. https://doi.org/10.2514/6.2013-2511

[43] Levy, D.W., Laflin, K.R., Tinoco, E.N., Vassberg, J.C., Mani, M., Rider, B., Rumsey, C.L., Wahls, R.A., Morrison, J.H., Brodersen, O.P., Crippa, S., Mavriplis, D.J., and Murayama, M., "Summary of Data from the Fifth Computational Fluid Dynamics Drag Prediction Workshop," *Journal of Aircraft*, Vol. 51, No. 4, 2014, pp. 1194–1213. https://doi.org/10.2514/1.C032389

[44] Torenbeek, E., *Synthesis of Subsonic Airplane Design*, 1st ed., Delft Univ. Press, Delft, The Netherlands, 1982.

[45] Raymer, D.P., *Aircraft Design: A Conceptual Approach*, 6th ed., AIAA, Reston, VA, 2018.

[46] Roskam, J., *Airplane Design Part V: Component Weight Estimation*, Fifth printing, DARcorporation, Lawrence, KS, 2018.

[47] Bradley, K.R., "A Sizing Methodology for the Conceptual Design of Blended-Wing-Body Transports," NASA CR-2004-213016, Sept. 2004.

[48] Velicki, A., and Jegley, D., "PRSEUS Development for the Hybrid Wing Body Aircraft," *AIAA Centennial of Naval Aviation Forum "100 Years of Achievement and Progress,"* AIAA Paper 2011-7025, Sept. 2021. https://doi.org/10.2514/6.2011-7025

[49] Mukhopadhyay, V., and Sorokach, M.R., "Composite Structure Modeling and Analysis of Advanced Aircraft Fuselage Concepts," *AIAA Modeling and Simulation Technologies Conference*, AIAA Paper 2015-3096, June 2015. https://doi.org/10.2514/6.2015-3096

[50] Gur, O., Bhatia, M., Mason, W.H., Schetz, J.A., Kapania, R.K., and Nam, T., "Development of a Framework for Truss-Braced Wing Conceptual MDO," *Structural and Multidisciplinary Optimization*, Vol. 44, No. 2, 2011, pp. 277–298. https://doi.org/10.1007/s00158-010-0612-9

[51] Anon., "Type-Certificate Data Sheet for PW1500G Series Engines," European Union Aviation Safety Agency, 24 Nov. 2022, https://www.easa.europa.eu/en/downloads/20863/en [retrieved 31 Jul. 2023].

[52] Cumpsty, N., Mavris, D., Alonso, J., Catalano, F., Eyers, C., Goutines, M., Grönstedt, T., Hileman, D.J., Joselzon, A., Khaletskii, I., Ogilvie, F., Ralph, M., Sabnis, D.J., Wahls, D.R., and Zingg, D., "Independent Expert Integrated Technology Goals Assessment and Review for Engines and Aircraft," International Civil Aviation Organization CAEP/11-WP/24, Feb. 2019.

[53] Anon., "14 CFR Part 25 Airworthiness Standards: Transport Category Airplanes," Federal Aviation Administration, 7 July 2023, https://www.ecfr.gov/current/title-14/chapter-I/subchapter-C/part-25?toc=1 [retrieved 27 Jul. 2023].

[54] Anon., "E-Jets-E2 Airport Planning Manual, APM-5824, Revision 21 - 05 AUGUST 2022," Embraer S.A., 22 Sept. 2017, https://www.flyembraer.com/irj/go/km/docs/download_center/Anonymous/Ergonomia/Home%20Page/Documents/APM_E-JetsE2.PDF [retrieved 15 Sep. 2023].

[55] Hicken, J.E., and Zingg, D.W., "A Simplified and Flexible Variant of GCROT for Solving Nonsymmetric Linear Systems," *SIAM Journal on Scientific Computing*, Vol. 32, No. 3, 2010, pp. 1672–1694. https://doi.org/10.1137/090754674

[56] Yin, F., Grewe, V., Castino, F., Rao, P., Matthes, S., Dahlmann, K., Dietmüller, S., Frömming, C., Yamashita, H., Peter, P., Klingaman, E., Shine, K.P., Lührs, B., and Linke, F., "Predicting the Climate Impact of Aviation for En-Route Emissions: The Algorithmic Climate Change Function Submodel ACCF 1.0 of EMAC 2.53," *Geoscientific Model Development*, Vol. 16, No. 11, 2023, pp. 3313–3334. https://doi.org/10.5194/gmd-16-3313-2023

[57] Torenbeek, E., *Advanced Aircraft Design: Conceptual Design, Analysis, and Optimization of Subsonic Civil Airplanes*, 1st ed., John Wiley & Sons, Inc., Chichester, U.K., 2013.

[58] Green, J.E., "Civil Aviation and the Environment – the next Frontier for the Aerodynamicist," *The Aeronautical Journal*, Vol. 110, No. 1110, 2006, pp. 469–486. https://doi.org/10.1017/S0001924000001378

[59] Green, J., "Laminar Flow Control - Back to the Future?," *38th Fluid Dynamics Conference and Exhibit*, AIAA Paper 2008-3738, June 2008. https://doi.org/10.2514/6.2008-3738

[60] Versprille, V.F.W., "Aerodynamic Shape Optimization of a Liquid-Hydrogen-Powered Blended-Wing-Body," Master's Thesis, Delft Univ. of Technology, Delft, The Netherlands, 2022.

[61] Perry, D.H., “An Analysis of Some Major Factors Involved in Normal Take-off Performance,” Aeronautical Research Council C.P. No. 1034, Dec. 1967.

[62] Hicken, J.E., and Zingg, D.W., “Induced-Drag Minimization of Nonplanar Geometries Based on the Euler Equations,” *AIAA Journal*, Vol. 48, No. 11, 2010, pp. 2564–2575. https://doi.org/10.2514/1.J050379

[63] Streuber, G.M., and Zingg, D.W., “Improved Dynamic Geometry Control Algorithms for Efficient Aerodynamic Shape Optimization,” *AIAA Journal*, Vol. 61, No. 5, 2023, pp. 2116–2134. https://doi.org/10.2514/1.J062132

[64] Sargeant, M.A., Hynes, T.P., Graham, W.R., Hileman, J.I., Drela, M., and Spakovszky, Z.S., “Stability of Hybrid-Wing-Body-Type Aircraft with Centerbody Leading-Edge Carving,” *Journal of Aircraft*, Vol. 47, No. 3, 2010, pp. 970–974. https://doi.org/10.2514/1.46544